Modelling of the ductile-brittle fracture transition in steel structures with large shell elements: a numerical study

Woongshik Nam [a, b, *], Odd Sture Hopperstad [c, d], Jørgen Amdahl [a, b]

[a] *Department of Marine Technology, Norwegian University of Science and Technology (NTNU), Norway*
[b] *Centre for Autonomous Marine Operations and Systems (AMOS), NTNU, Norway*
[c] *Structural Impact Laboratory (SIMLab), Department of Structural Engineering, NTNU, Norway*
[d] *Centre for Advanced Structural Analysis (CASA), NTNU, Norway*

Abstract

In this paper, the strain energy density (SED) criterion is proposed for predicting the ductile-brittle fracture transition (DBFT) in ships and offshore structures. In finite element simulations, these structures are discretized by relatively large shell elements which precludes the modelling of the local stress and strain states in the vicinity of a crack. Critical values of the SED are determined based on local simulations of fracture for a range of temperatures and plane stress states. The local simulations of fracture are based on combined use of the Gurson model for ductile damage and fracture and the Richie-Knott-Rice (RKR) criterion for brittle fracture. After calibrating the Gurson model and the RKR criterion to existing experiments on offshore steel, critical values of the SED are found by analysing a representative plate element with a generic through-thickness crack using a refined solid element mesh. The proposed failure model is evaluated by simulating drop tests on steel-plated structures found in the literature. The present study indicates that the SED criterion is a useful concept for practical design of ships and offshore structures at sub-zero temperatures, but further assessment against experimental data is necessary to fully establish its credibility.

Key words: Ductile-brittle failure transition for steel; Arctic temperatures and cryogenic spills; Analysis with shell elements; Global approach to failure; Strain energy density criterion;

1 Introduction

Crashworthiness is an important issue in the design of ships and offshore structures to meet safety level requirements. Despite of the worldwide effort to prevent accidents in the oceans, an average number of 23.8 collisions per year is reported by the international maritime organization in the last 10 years [1]. These collisions often lead to enormous damage in terms of environmental pollution and economic loss, and sometimes even loss of life. To avoid severe casualties, ship classifications societies and authorities recommend criteria to be considered and applied in the design of ships and offshore structures. For accidental actions, the design must be carried out following the principles of Accidental Limit State (ALS) design. In ALS design, substantial damage to the target structure (or the struck structure) is tolerated after the action of the abnormal event, but the damage should not result in progressive degradation of the structural integrity. Based on the ALS scenarios, the design of ships and offshore structures needs experimental tests and

numerical analyses to examine the crashworthiness. It is practically impossible to conduct large scale experiments on real structures and small scale experiments often have limited validity for direct application in the design because the test setup only approximately realizes the true nature of the problem. Thus, it is necessary to resort to numerical simulations in the design of these structures. There has been a rapid development of computer capacity and nonlinear finite element analysis (NLFEA) methods in the past decades, and several commercial NLFEA codes are available. These codes have improved greatly the ability of engineers and designers to perform numerical analyses of the response of marine structures to accidental actions. The damage obtained by simulation of an accidental action such as a ship collision is critically influenced by the mechanical properties of the material, the finite element mesh size, the modelling of material failure and even the expertise of the engineers performing the simulations, e.g. Paik [2], Ehlers [3], Ehlers and Østby [4], Högstrom and Ringsverg [5], Choung et al. [6], and Storheim and Amdahl [7]. The material characteristics include yield strength, Lüders plateau, strain hardening, damage softening, as well as the effects of strain rate and temperature.

In the past few decades, we have seen significant increase in Arctic activities partly due to global warming, e.g. marine transport along the northern sea route (NSR) and extraction of natural resources such as oil and gas. While the decrease of the ice cover in Arctic regions may provide substantial economic benefit, structures operating in these regions are exposed to harsh environmental conditions, particularly sub-zero temperatures (average -50℃) and the risk of iceberg impact. The crashworthiness of structures for such events should be confirmed in the design phase, but proper design guidelines for modelling of material behaviour at low temperatures are lacking.

High-strength steel has been used by the shipbuilding industry in ships made for the Arctic environment. Ehlers and Østby [4] and Park et al. [8] conducted numerical analyses to investigate the resistance of high-strength steel structures subjected to Arctic temperatures. Figure 1 shows results from tensile tests on a high-strength steel. The engineering failure strain increases with decreasing temperature as do the yield stress and the ultimate stress, and there is an apparent increase in the energy absorption capability of the material at lower temperature. In Ehlers and Østby [4] and Park et al. [8], the simulations were based entirely on the result of quasi-static uniaxial tensile tests (cf. Figure 1). Local failure was predicted by a ductile fracture criterion, while the possibility of brittle fracture was not considered explicitly. These authors concluded that structures built with high-strength steel have more strength in Arctic regions. This contradicts general experience; with temperatures down to -50℃ in Arctic regions the ductile-brittle transition temperature (DBTT) could be reached and thus induce brittle fracture during abnormal events.

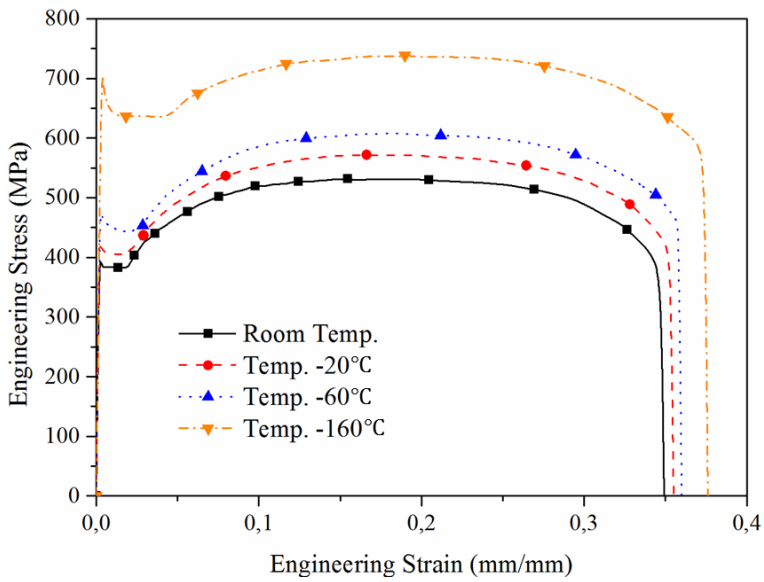

Figure 1. Engineering stress-strain curves of the high-strength steel DH36 at several temperatures, reproduced from Park et al. [9].

Examples of abnormal events that could induce brittle fracture in offshore structures are collision with other structures or icebergs in extreme Arctic temperatures (in the range of –50°C) as well as cryogenic spills (liquid natural gas), where the steel temperature may become even lower. Owing to the lack of relevant experimental data, numerical studies of large-scale structures should be performed to investigate the consequences of such events. There is, therefore, a need for an accurate, efficient and robust modelling framework to analyse numerically the ductile-brittle fracture transition in large-scale structures. To this end, Nam et al. [10] performed numerical simulations of Charpy V-notch tests of a high-strength steel presented by Min et al. [11]. The Charpy V-notch tests were conducted at temperature from 20°C to -160°C, and fracture transition was observed at -40°C to -50°C both in the experiments and the numerical simulations. In the simulation of these tests, a shear failure criterion was used to model ductile fracture, while the RKR criterion proposed by Ritchie, Knott and Rice [12] was used for brittle fracture. Isothermal and rate-independent von Mises plasticity was used to describe the material behaviour while accounting for the influence of temperature on the yield strength and strain hardening. It was found that the combined use of the shear failure criterion for ductile fracture and the RKR criterion for brittle fracture successfully described the ductile-to-brittle transition observed in the Charpy V-notch tests, while the shear failure criterion alone would significantly overestimate the crashworthiness of structures built by high-strength steel at low temperatures.

The change of the local fracture mode from ductile to brittle depends on several factors such as the ambient temperature, the strain rate and the stress state. Ductile-to-brittle fracture transition (DBFT) studies have been presented in several papers, e.g. Tvergaard and Needleman [13, 14], Needleman and Tvergaard [15], Batra and Lear [16], Hütter et al. [17] and Türtük and Deliktas [18]. In [15], the ductile-brittle transition was simulated numerically using the Gurson model [19]

to describe ductile damage and the RKR criterion [12] to model cleavage. The Gurson model [19] describes porous plasticity by introducing the void volume fraction as the single damage variable which evolves with plastic straining as a function of the stress state. Chu and Needleman [20] introduced strain- or stress-driven void nucleation and later Tvergaard and Needleman [21] used the nucleation laws to enhance the ductile failure process that is associated with nucleation, growth and coalescence of voids. The result was the so-called GTN model. In the recent years, numerous modifications of the GTN model have been proposed [22-24] to account for the shear effects on damage evolution, i.e., shear localization and failure in the range of low stress triaxiality, $0 \leq \eta < 1/3$. While Gurson-type porous plasticity models are typically used for ductile fracture, a number of brittle fracture models have been proposed, e.g. Ritchie et al. [12], Beremin [25], Wallin [26], and Minami et al. [27]. Based on the Weibull theory, Beremin [25], Wallin [26] and Minami et al. [27] used a statistical approach to account for the unavoidable scatter of the fracture toughness. The RKR criterion [12] is based on the assumption that brittle fracture occurs when the major principal stress σ_1 exceeds a critical value σ_c over a characteristic distance l_c, where σ_c could be taken as a random variable to account for statistical scatter. These models are all based on a local approach to fracture, which requires detailed information about the microstructure of the material. The characteristic length l_c of the process zone, in which the damage mechanisms occur, calls for an element size corresponding to the size of a few grains [12], thus leading to excessive calculation times in NLFEA of structural systems. Consequently, it is difficult to apply this micromechanical approach to fracture in large-scale simulation of ships and offshore structures in the ALS. As an alternative, more global approaches to fracture of structural steel have been developed for use in coarsely meshed structures and verified by comparison with test results. Some examples are the RTCL criterion [28], the T criterion [29], the modified Mohr-Coulomb (MMC) criterion [30], the BWH instability criterion [31], and the extended BWH criterion [32]. However, these global criteria are developed only to model ductile fracture of structures and a global criterion also describing failure at low temperatures is required.

In the presence of a crack, fracture mechanics criteria such as the stress intensity factor K or the J-integral could be used. However, these criteria are based on the local stress and strain states around the crack tip, and the use of them must be restricted carefully according to the extent of the local plastic deformations. Large shell elements cannot capture the detailed local states properly and thus local failure initiation and subsequent propagation as well. Alternatively, we propose to use the strain energy density (SED) criterion to model failure in steel structures at low temperatures, thus accounting in a simplified manner for both ductile and *more brittle failure* modes. The advantage of the SED criterion is that the material resistance to failure is expressed by the elastic and plastic energy contributions for a given temperature and stress state in a simple and practical way. In practice, the elastic energy density is important for failure only at temperatures below DBFT, whereas the plastic energy density plays the major role at higher temperatures. The SED criterion is calibrated from local simulations of fracture using the Gurson porous plasticity model [21] for ductile fracture in combination with the RKR criterion [12] for brittle fracture. Available experimental data for the high-strength steel DH36, according to the designation of steel grades by DNV [33], is used in all simulations. First, we investigate the fracture toughness of the high-

strength steel as a function of the temperature and the fracture probability level based on three-point bending test data provided by Sumpter and Kent [34]. Numerical simulations of tensile and three-point bending tests are performed to determine the parameters of the Gurson model and the RKR criterion, respectively. Second, we conduct calibration of the SED criterion by means of numerical simulations to bridge the gap between the fine solid element model required in the local fracture analysis and the large shell element model required in the structural analysis with respect to predicting failure at a range of temperatures from 20℃ to -160℃. To this end, a high-strength steel plate element with a generic through-thickness crack is subjected to proportional tensile loading ranging from uniaxial tension to equi-biaxial tension. The plate element is modelled with a fine solid element mesh and the Gurson model is used in combination with the RKR criterion to model fracture. These local simulations are then used to calibrate the SED criterion for a range of temperatures and stress states, adopting von Mises plasticity. The proposed failure model is finally evaluated by NLFEA simulations and comparisons with impact tests of steel-plated structure at low temperatures performed by Park et al. [9] and Kim et al. [35].

2 Material modelling

2.1 Local approach to failure

In the local approach to failure, we combine the modified Gurson model for ductile fracture with the RKR model for brittle fracture as proposed in [13-15]. The modified Gurson yield function is given by [21, 36]

$$\Phi(\boldsymbol{\sigma}, f, \sigma_M) = \frac{\sigma_{eq}^2}{\sigma_M^2} + 2q_1 f \cosh\left(\frac{3q_2\sigma_H}{2\sigma_M}\right) - (1 + q_3 f^2) \leq 0 \tag{1}$$

where $\boldsymbol{\sigma}$ is the stress tensor, f is the void volume fraction, σ_M is the flow stress of the matrix material, $\sigma_{eq} = \sqrt{\frac{3}{2}\mathbf{s}:\mathbf{s}}$ is the von Mises equivalent stress, $\mathbf{s} = \boldsymbol{\sigma} - \sigma_H\mathbf{I}$ is the stress deviator, $\sigma_H = \frac{1}{3}\mathrm{tr}(\boldsymbol{\sigma})$ is the hydrostatic stress, $\mathbf{I}$ is the second-order unit tensor, and q_1, q_2 and q_3 are model constants introduced in [36]. The associated flow rule is adopted to describe the plastic flow of the porous material, and the evolution of the void volume fraction f is determined by assuming that the plastic flow of the matrix material is isochoric. The initial void volume fraction is f_0 and, for simplicity, we neglect nucleation of new voids and void softening in shear, and assume that failure occurs by void coalescence at a critical void volume fraction, f_c. This is assumed to be a reasonable assumption because the local failure occurs very abruptly after the void volume fraction exceeds the critical value f_c [37]. The constants q_1, q_2 and q_3 are given the values proposed in [36]: $q_1 = 1.5$, $q_2 = 1.0$ and $q_3 = q_1^2$. The reader is referred to e.g. [21] and [36] for more details on the modified Gurson model.

The RKR model [12] assumes that cleavage fracture initiates and propagates once the local maximum principal stress σ_1 exceeds a critical value σ_c over a characteristic length l_c. The characteristic length is commonly taken to be a few times the grain size of the material. The critical

stress σ_c is assumed independent of temperature and strain rate [38, 39]. As already mentioned, statistical approaches based on the Weibull theory have been proposed to account for the scatter observed for brittle fracture modes [21][22][25]. However, as the objective of the current study is to evaluate the potential of the proposed modelling strategy, a deterministic approach has been adopted while the statistical approach is left for future work.

Thus, in the local approach to fracture adopted here, the flow stress of the matrix material σ_M is fitted to experimental data for each temperature while the other parameters, namely, f_0, f_c, σ_c and l_c, are assumed constant.

2.2 Global approach to failure

In the large shell simulations of structures, we combine von Mises plasticity (i.e., the von Mises yield criterion, the associated flow rule and isotropic hardening) with the SED criterion. The flow stress of the material is fitted to experimental data obtained at each temperature, while the SED criterion is a function of both temperature and stress state. The SED criterion proposed by Sih [40] has been employed successfully to predict brittle behaviour at the crack tip in a local approach to fracture [40-43]. On the macroscopic scale, the plastic strain energy density failure criterion has been used in analyses of beams and circular plates with dynamic loads [44, 45].

In this study, we assume that the large shell element fails when the distortional part of the strain energy density w reaches a critical value, $w_c(\beta, T)$, which is taken to depend on the stress state through the strain increment ratio β as well as the temperature T. Assuming plane stress states, β is defined by

$$\beta = \frac{d\varepsilon_2^p}{d\varepsilon_1^p} \tag{2}$$

where $d\varepsilon_1^p$ and $d\varepsilon_2^p$ are the major and minor in-plane plastic strain increments. Owing to the associated flow rule, β characterizes the stress state of the material. In particular, β equals unity for equi-biaxial tension, zero for plane-strain tension and $-\frac{1}{2}$ for uniaxial tension.

The distortional part of the strain energy density is calculated as

$$w = \int \mathbf{s} : d\boldsymbol{\varepsilon} \tag{3}$$

where $d\boldsymbol{\varepsilon}$ is the incremental strain tensor. The failure criterion for the material is then expressed as

$$w = w_c(\beta, T) \tag{4}$$

Using the additive decomposition of the incremental strain tensor into elastic and plastic parts, $d\boldsymbol{\varepsilon} = d\boldsymbol{\varepsilon}^e + d\boldsymbol{\varepsilon}^p$, the elastic and plastic parts of $w = w^e + w^p$ are defined by

$$w^e = \int \mathbf{s} : d\boldsymbol{\varepsilon}^e, \;\; w^p = \int \mathbf{s} : d\boldsymbol{\varepsilon}^p \tag{5}$$

The elastic part is path independent, and for an isotropic material it can be expressed as

$$w^e = \frac{1+\nu}{3E}\sigma_{eq}^2 \tag{6}$$

where E is Young's modulus and ν is Poisson's ratio. In contrast, the plastic part is path dependent and expressed in integral form as

$$w^p = \int \sigma_{eq} d\varepsilon_{eq}^p \tag{7}$$

where $d\varepsilon_{eq}^p = \sqrt{\frac{2}{3} d\boldsymbol{\varepsilon}^p : d\boldsymbol{\varepsilon}^p}$ is the incremental equivalent von Mises strain.

In addition to the SED criterion, the BWH criterion proposed by Alsos et al. [31] is used to estimate the onset of local necking (or plastic instability)

$$\sigma_1 = \begin{cases} \dfrac{2k}{\sqrt{3}} \dfrac{1+\frac{1}{2}\beta}{\sqrt{\beta^2+\beta+1}} \left(\dfrac{2}{\sqrt{3}} \dfrac{n}{1+\beta} \sqrt{\beta^2+\beta+1} \right)^n & \text{for} \quad -1 < \beta \leq 0 \\ \dfrac{2k}{\sqrt{3}} \dfrac{\left(\frac{2}{\sqrt{3}} n \right)^n}{\sqrt{1-(\beta/(2+\beta))^2}} & \text{for} \quad 0 < \beta \leq 1 \end{cases} \tag{8}$$

where σ_1 is major principal stress. The parameters k and n are the power-law parameters defined in Table 1. It is noted that the failure of elements in subsequent numerical simulations is governed only by the SED criterion. The SED criterion is checked in all through-thickness integration points, while the BWH criterion is only evaluated in the middle through-thickness integration point of the shell element, as it only applies to membrane stresses and strains.

3 Calibration of the Gurson model

In the Gurson model adopted here, we need to calibrate the initial and critical void volume fractions f_0 and f_c, respectively. To this end, numerical simulation of the tensile test in [9] is performed using ABAQUS/implicit in which the Gurson yield function is applied without considering the accelerated void growth after void coalescence, i.e., failure is assumed to occur when f equals f_c. The mid-section in which material failure is expected to occur is discretized with fine solid elements (C3D8R) of 0.16 mm characteristic length. This element size is equal to the assumed characteristic length l_c of the RKR criterion for the investigated material, see discussion in Section 4. Outside the gauge region the specimen is coarsely meshed to reduce the computation time. The material properties of DH36 steel are given in by Park et al. [9]. The engineering stress-strain curves are shown in Figure 1, whereas the true stress-strain curves

representing the matrix flow stress in the simulations are plotted in Figure 2. The material properties and hardening parameters of DH36 steel are summarized in Table 1, where σ_Y is the initial yield stress, s_T is the tensile stress, ε_L is the is the equivalent plastic strain at the exit of the Lüders plateau, and e_f is the engineering strain at failure. The work hardening rule is defined as

$$\sigma_M = \begin{cases} \sigma_Y & \text{for} \quad \varepsilon_M \leq \varepsilon_L \\ k(\varepsilon_M - \varepsilon_0)^n & \text{for} \quad \varepsilon_M > \varepsilon_L \end{cases} \tag{9}$$

where ε_M is the equivalent plastic strain of the matrix material (see [36] for the definition), k and n are hardening parameters, and

$$\varepsilon_0 = \varepsilon_L - \left(\frac{\sigma_Y}{k}\right)^{\frac{1}{n}} \tag{10}$$

It should be noted that the given material parameters will be used in all subsequent numerical analyses in the present paper, and, if necessary, the material behaviour at intermediate temperatures is simulated by interpolation.

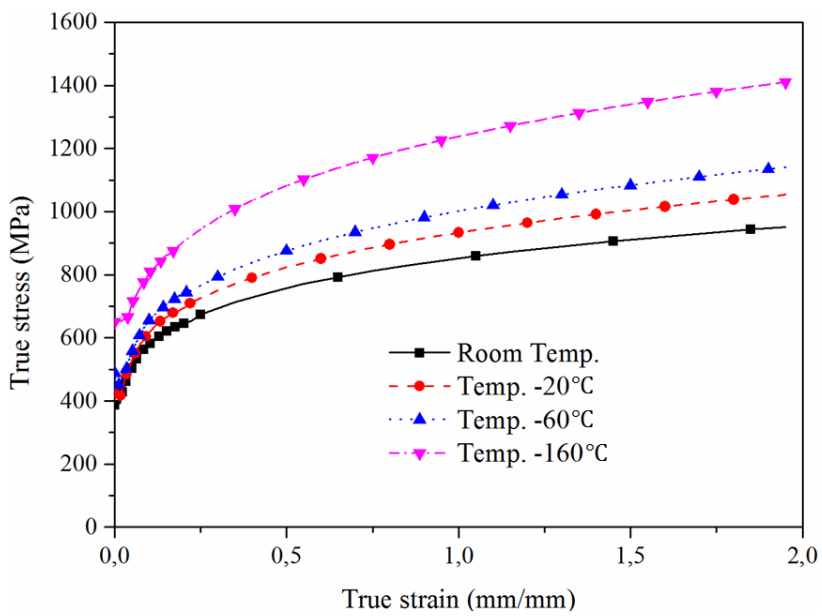

Figure 2. True stress-strain curves of DH36 steel.

The initial void volume fraction f_0 is set equal to 0.002 [46]. The void growth was investigated in an element placed at the centre of the mid-section of the specimen where the failure is expected to occur. Subsequently, the critical void volume fraction f_c was found in the element when the engineering strain of the specimen reaches the failure strain. Based on the simulation of the tension test at room temperature, the critical void volume fraction f_c was determined to be

0.01. Simulations of the tensile tests at the other temperatures were then conducted with $f_c = 0.01$, and the experimental and simulated engineering stress-strain curves are compared in Figure 3. Even if there are small deviations (error within 2.8%) between the experimental and predicted failure strains at the lower temperatures, the calibrated Gurson model is considered to have the required accuracy to model ductile failure regardless of temperature and is employed in the subsequent simulations of the ductile-brittle fracture transition.

Table 1. Material properties obtained from uniaxial quasi-static tensile test of DH36 steel.

T (°C)	σ_Y (MPa)	s_T (MPa)	ε_L (%)	e_f (%)	n	k (MPa)
20	383	530	2.1	34.8	0.167	851
-20	406	569	1.9	35.3	0.181	933
-60	443	606	2.9	35.8	0.194	1002
-160	636	735	4.4	37.4	0.195	1238

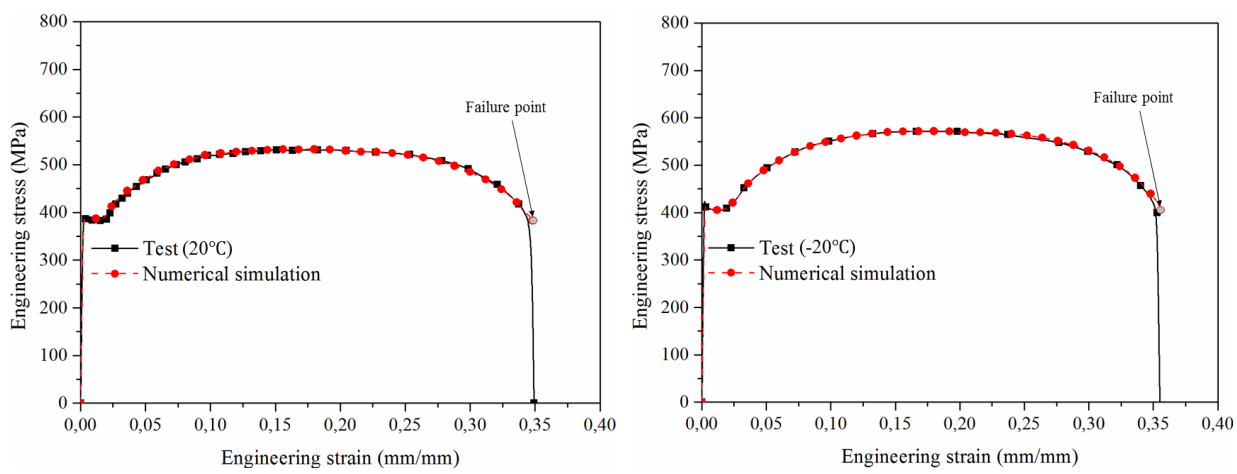

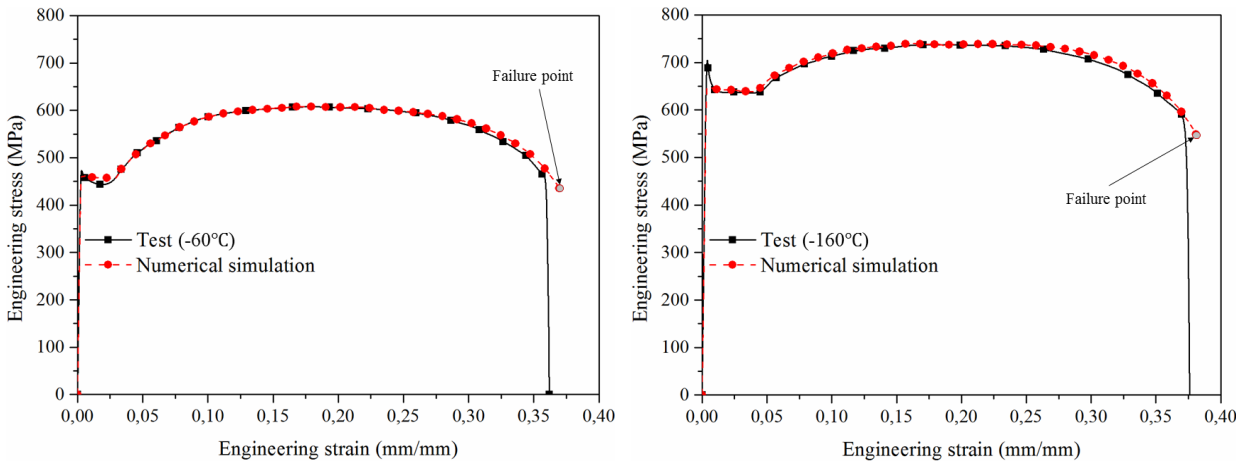

Figure 3. Experimental and simulated engineering stress-strain curves with ductile failure for DH36 steel.

4 Calibration of the RKR criterion

Only a few fracture mechanics tests have been conducted to obtain the critical stress intensity factor for marine structural steel [34]. The reason for this is twofold: first, accidents by brittle fracture in ships and offshore structures have been rarely reported in recent decades [47], and second, the Charpy-V test is preferably employed to examine toughness of the steel as function of temperature due to its simplicity and intuitiveness. Sumpter and Kent [34] carried out three-point bending tests of 15 mm thick high strength steel at various temperatures. They estimated the fracture toughness and the fracture probability level as a function of the temperature. We selectively use the fracture toughness data in [34] for D-grade and DH-grade steel. Both steels correspond to the target material in this study. We have adopted the same procedure as in [34] to find the fracture toughness curves for a given probability level. A best fit to the data is obtained by the exponential curve fit (ECF) method. The reader is referred to [34] for all the test data, details of the test procedures and a description of the ECF method. Figure 4 shows the fracture toughness of D-grade and DH-grade steel in terms of the relative temperature $T - T_{27J}$ as a function of the probability level for fracture toughness, where T_{27J} is the Charpy 27 J transition temperature.

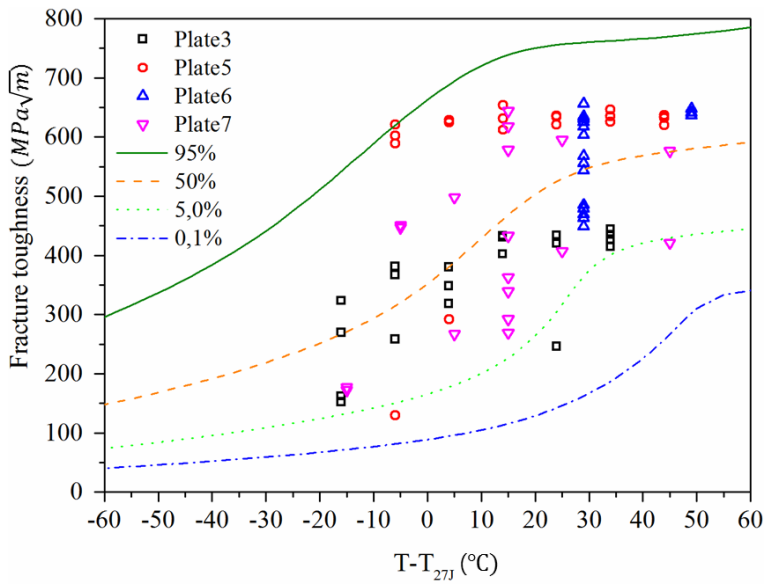

Figure 4. Exponential curve fit of fracture toughness data with different probability level for fracture toughness, based on the experimental results in [32]. The fracture toughness is defined as $K_{Jc} = \sqrt{EJ_c}$, where E is Young's modulus and J_c is the critical value of the J-integral.

Numerical simulations of the three-point bending tests presented in [34] are conducted using ABAQUS/implicit. The Gurson model and the RKR criterion are used in these simulations with the aim to determine the critical stress σ_c in the RKR criterion for the D-grade steel. The J-integral of an elastic-plastic material can be computed in the simulations and converted to the stress intensity factor by $K_J = \sqrt{EJ}$ [48], where E is Young's modulus. Accordingly, the critical stress intensity factor is given by $K_{Jc} = \sqrt{EJ_c}$, where J_c is the critical value of the J-integral. In [12] and [49], the grain size of mild steels is reported to be $60\ \mu\text{m}$ and $70\ \mu\text{m}$, respectively. For brittle fracture to occur, the critical stress must be attained over a region with extension defined by the characteristic length l_c of the process zone, which should be taken as the size of some few grains [12]. In view of this, we set the characteristic length to $l_c = 0.16\ \text{mm}$ and adopt a characteristic element size equal to l_c. The remaining parts of the specimen are discretized by a relatively coarse mesh to reduce the computation time, see Figure 5. We use the two-dimensional continuum element CPE4R, which is a four-node plane-strain element with reduced integration and hourglass control. A static friction coefficient of 0.3 is assigned for contact between the rollers and the specimen.

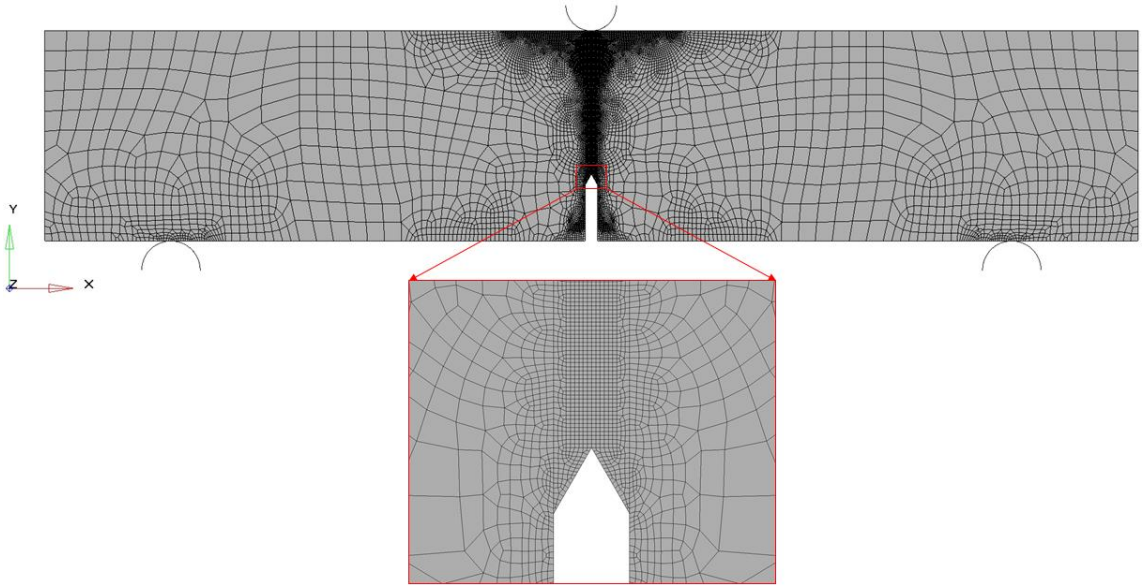

Figure 5. Finite element mesh of the three-point bending specimen. The specimen has thickness $B = 15$ mm, width $W = 50$ mm, crack length $a = 15$ mm, and ligament $b = 35$ mm, whereas the span between the supports is $S = 200$ mm.

The fracture toughness is evaluated in elements located in the mid-span of the specimen. Crack initiation is assumed when the maximum principal stress exceeds the critical stress value σ_c or when the critical void volume fraction f_c is reached. In other words, if an element reaches σ_c prior to f_c, we consider brittle fracture to occur in the specimen, else the fracture is signified as ductile. We use f_c equal to 0.01 as determined in section 3, while three critical values of σ_c, namely 1340, 1400 and 1450 MPa, are applied in the simulations. The simulation results are shown in Figure 6. It is seen that the adopted modelling approach is capable of predicting the fracture toughness as a function of temperature with reasonable accuracy. The simulated toughness curves are all rather close to 50 percent level of the fracture toughness. However, to be conservative, we adopt σ_c equal to 1340 MPa, which is about 3.5 times the yield stress at room temperature.

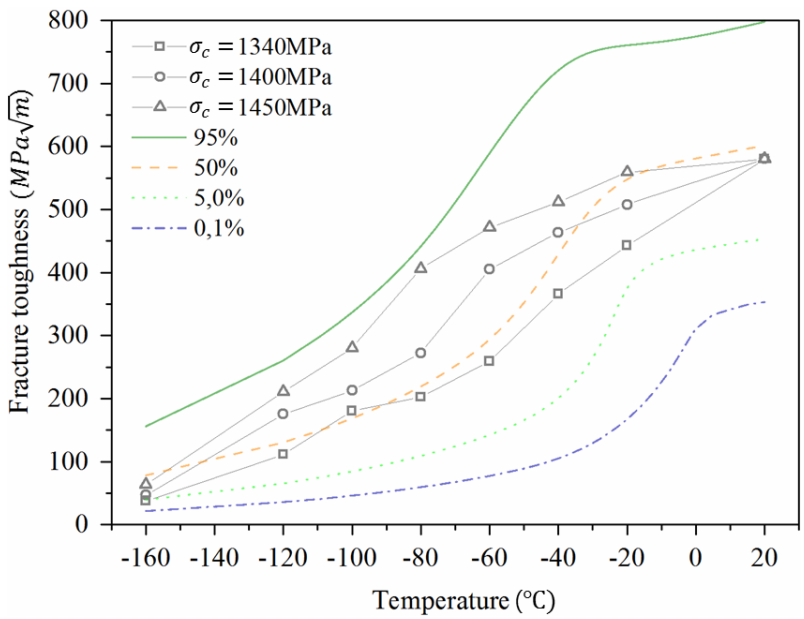

Figure 6. Numerical fracture toughness curves in terms of K_{Jc} compared with exponential curve fits of fracture toughness data with different probability levels.

5 Calibration of the SED criterion

5.1 Simulations of fictitious plates

This section describes the calibration of the strain energy density (SED) criterion for large shell elements. To this end, numerical simulations are performed with the two fictitious plate models shown in Figure 7. We create a finite element model of a square plate with 70 mm width and 10 mm thickness because analysis of energy dissipation in large-scale structures is normally performed with shell elements having a length of 5 to 10 times the plate thickness [50]. The first fictitious plate (P1) is modelled by only one large shell element, which is the quadrilateral finite-membrane-strain shell element with reduced integration (S4R). The second plate (P2) consists of a very fine mesh of solid elements in the expected failure region, namely the hexahedral solid elements with eight nodes and reduced integration (C3D8R). The mesh size of the solid elements is about 0.16 mm to comply with the characteristic length of the RKR model. Plate P2 includes an initial sharp crack at the centre. The initial crack models an imperfection of the plate which may come from a welding process and/or various operations of the structures. The initial crack length through thickness introduced in plate P2 is 1.6 mm with the ratio between the crack length a and the plate width w equal to $a/w \approx 0.02$. Very limited information of actual initial crack lengths is available in the literature. Mai et al. [51], Moan [52], Ziegler et al. [53], Akpan [54], Bokalrud and Karlsen [55], Kountouris and Baker [56] and Kirkemo [57] used an exponential distribution for the initial defect size with the mean value in the range from 0.11 mm to 0.94 mm. Based on this, the initial crack size of 1.6 mm adopted in this study seems to be fairly conservative. However, in order to demonstrate the potential of the proposed modelling approach, the crack length is selected so that brittle fracture is generated in the simulations at the lower temperatures.

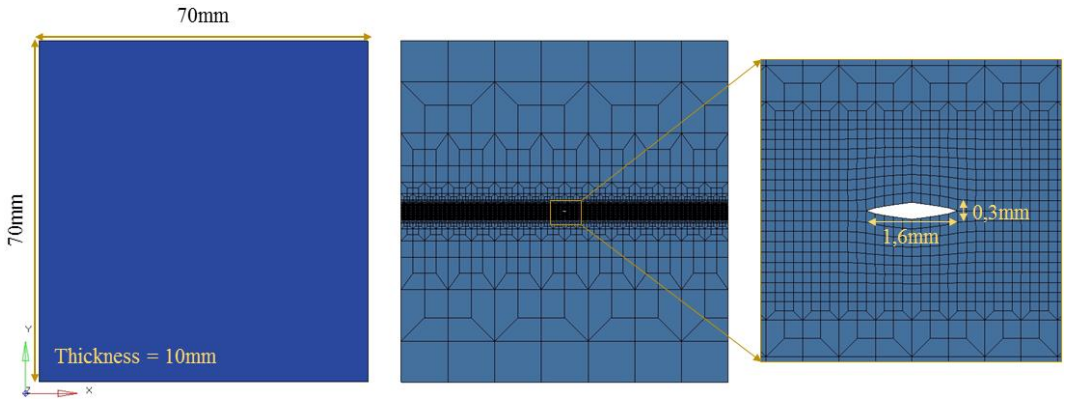

Figure 7. FE models of two fictitious plates: P1 (left) and P2 (middle and right).

We perform the simulations by assigning a quasi-static biaxial tensile loading to the plates. The effects of strain rate are neglected in the modelling of the stress-strain behaviour and the local approach to failure, and thus in the calibration of the SED criterion. In analysis of structures by means of numerical simulations, we need to have accurate information of all essential parameters for best possible verification of the method. For design purposes, the situation is somewhat different. We may specify a characteristic crack length that leads to characteristic strain energy density levels at fracture. The crack length may not be the "true" one, but realistic and reasonably conservative dependent on model uncertainties, such as stress concentration factors, strain rate effects and statistical aspects of fracture. The same situation is encountered in many other design situations; e.g. many design codes present column-buckling curves that are based upon equivalent imperfections, where both the magnitude and the shape are not the "true" ones. Thus, a design crack could be specified for application of this method. The design crack length should not be changed for one design check to the other, but remain constant. If the local model is improved or more data become available, the design crack length could be adjusted (probably reduced) to reflect the improvement of the basis for the method.

The simulations of plate P2 are regarded as numerical experiments and used to calibrate the SED criterion for a range of stress states and temperatures. In plate P2, crack initiation and propagation are predicted by the local approach to failure. The Gurson model is used for ductile failure and the RKR criterion for brittle failure with the critical material parameters f_c and σ_c determined above. One simulation of plate P2 requires approximately 20 CPU hours on a super computing system. The range of temperature studied in these simulations is from room temperature, $T = 20℃$, to cryogenic temperature, $T = -160℃$. It is reported that the stress state in failed elements in ship impact analyses is mostly within the range of moderate stress triaxiality, $1/3 \leq \eta \leq 2/3$ [58] such that we assign a series of proportional loading paths, i.e., with constant β, from uniaxial tension ($\beta = -0.5,\ \eta = 1/3$) to equi-biaxial tension ($\beta = 1,\ \eta = 2/3$) for both plates. We assume that complete failure of plate P2 occurs once the crack has propagated by element erosion over the entire width to reach the two vertical edges, see Figure 8.

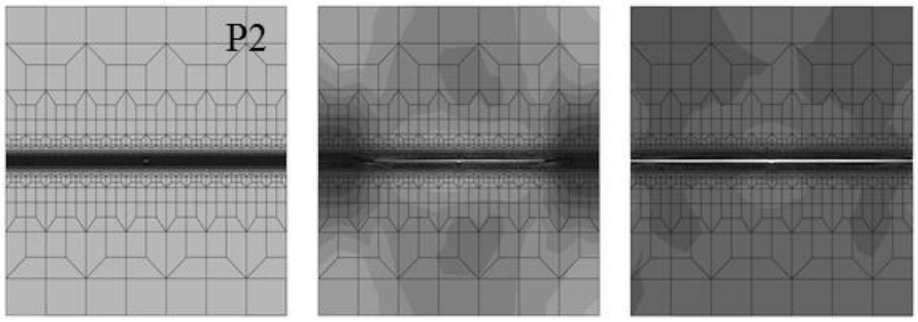

Figure 8. Illustration of crack propagation to complete failure of plate P2: (1) Plate with initial crack; (2) Crack propagation; (3) Final fracture of the plate.

The response of the two plates P1 and P2 in plane-strain tension is illustrated in Figure 9 in terms of the engineering stress-strain curves in the direction normal to the crack propagation. The initial through-thickness crack barely influences the stress level, but has an impact on the failure strain. In addition, the strain energy density of plate P1 is reported at the time of local failure initiation, t_{init}, and failure termination, t_{term}, in plate P2, see Table 2. A relatively large increase of the distortional strain energy is needed to propagate the crack through the plate at room temperature, while the energy dissipation associated with crack propagation is negligible at lower temperatures. Except at the two lowest temperatures, where the fracture is brittle, the elastic distortional strain energy density w^e is very small compared to the total distortional strain energy density, $w = w_c$, at full failure.

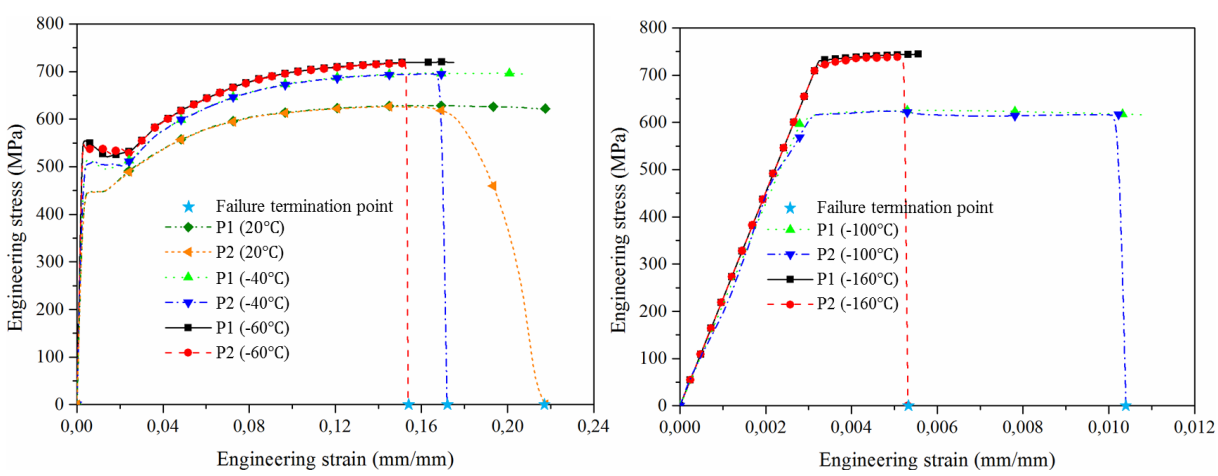

Figure 9. Engineering stress-strain curves for plates P1 and P2 for plane-strain tension ($\beta = 0$) with indication of fracture. Plate P2 exhibits ductile failure at room temperature, brittle failure at -100℃ and -160℃, a mixed failure mode between -20℃ and -60℃.

Table 2. Elastic, plastic and total distortional strain energy densities (in MPa) in plate P1 at failure initiation, t_{init}, and failure termination, t_{term}, in plate P2.

Temperature	t_{init}			t_{term}		
	w^e	w^p	w	w^e	w^p	w
20°C	0.8	93.3	94.1	0.9	124.8	125.7
-40°C	1.0	107.5	108.5	1.0	109.3	110.3
-60°C	1.1	105.6	106.7	1.1	106.1	107.2
-100°C	0.6	4.2	4.8	0.6	4.3	5.0
-160°C	0.9	1.3	2.2	0.9	1.4	2.3

The strain energy density w in plate P1 at complete failure of plate P2 is taken as the critical value w_c for a given temperature T and strain increment ratio β. The results are presented in Figure 10, which shows the strong dependence of w_c on both T and β. The fracture mode seems to change from ductile to brittle at some temperature between -60°C and -100°C, while for higher temperatures, the void volume fraction f in some elements ahead of the initial crack tip exceeds the critical value f_c before the major principal stress σ_1 reaches the critical stress σ_c. In plate P2, we observe ductile failure at room temperature and brittle failure at temperatures lower than -100°C regardless of the stress state, while mixed failure modes are found for temperatures between -20°C and -60°C. It is evident from Figure 10 that there is a sufficient number of calibration points to develop an analytical representation of the fracture curve $w_c(\beta)$ at each temperature T. An exponential function is used to represent $w_c(\beta)$ over the entire range of β-values analyzed. The fracture loci for all temperatures obtained are gathered in Figure 11. As expected, we find that w_c is consistently reduced with decreasing temperature. It is further observed that the plate has less ductility in plane-strain tension ($\beta = 0$) than for uniaxial tension ($\beta = -0.5$) and equi-biaxial tension ($\beta = 1$).

Another way of illustrating the effect of temperature, stress state and failure mode is to use the Keeler-Goodwin diagram [59, 60], which is a so-called strain-based forming limit diagram (FLD). However, in our case the FLD should be read as a failure limit diagram, as we are not considering formability in the ordinary sense. The failure limit curves obtained by the SED criterion are shown in Figure 12. The abrupt reduction in ductility when the temperature is decreased below -60°C is clearly evident in the figure. The strong influence of the stress state is also seen with the lowest ductility occurring for plane-strain tension.

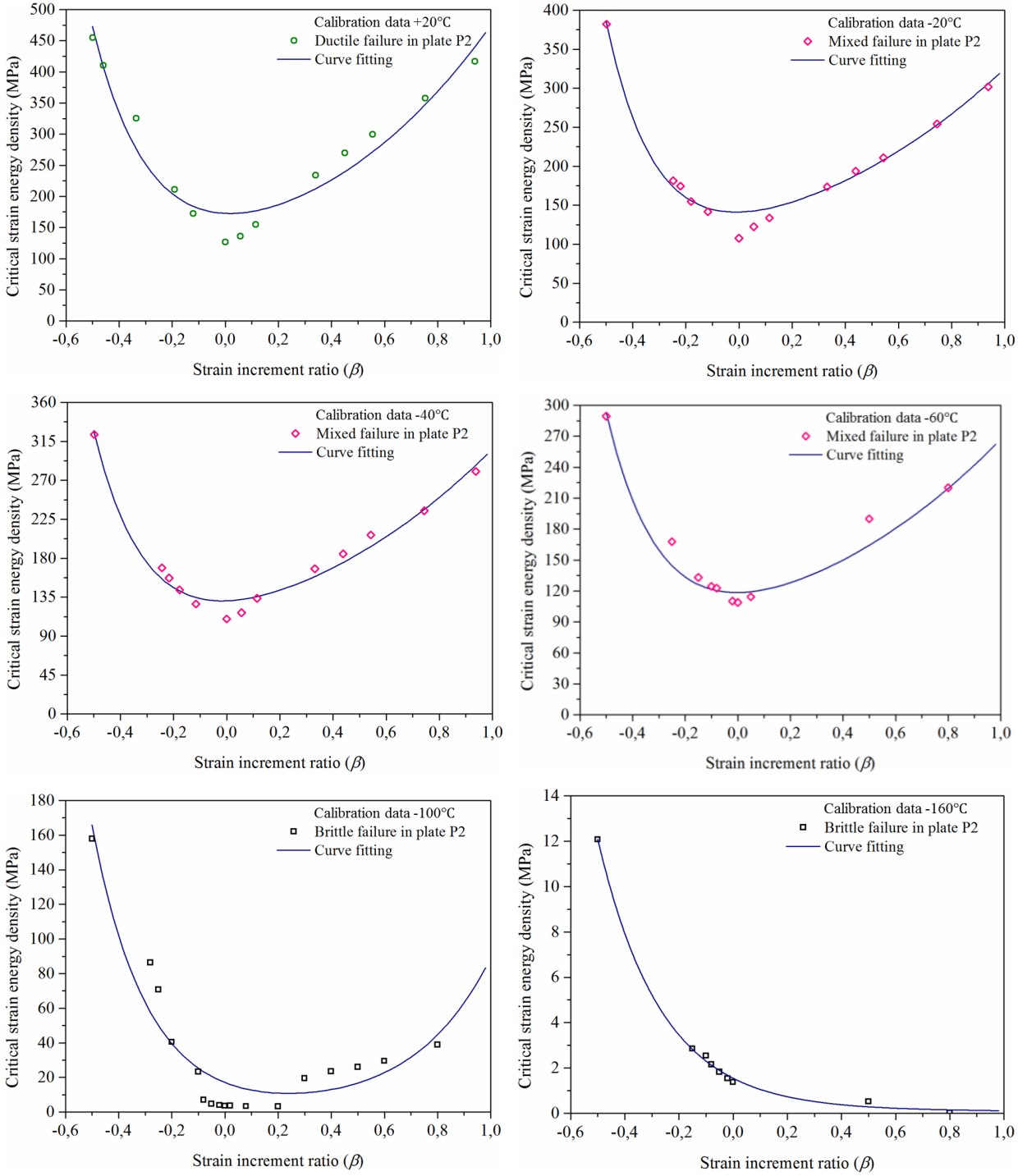

Figure 10. Calibration of the SED failure criterion, $w = w_c(\beta)$, at different temperatures T based on numerical simulations with the Gurson model and the RKR criterion.

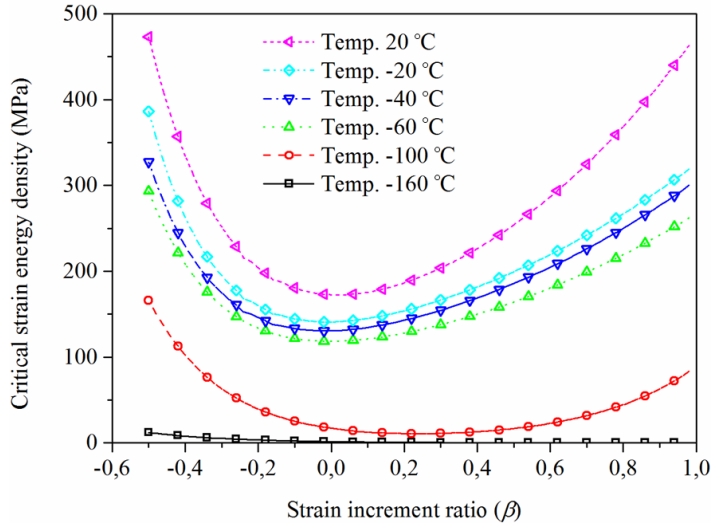

Figure 11. Fracture loci $w_c(\beta)$ for temperatures between $20℃$ and $-160℃$.

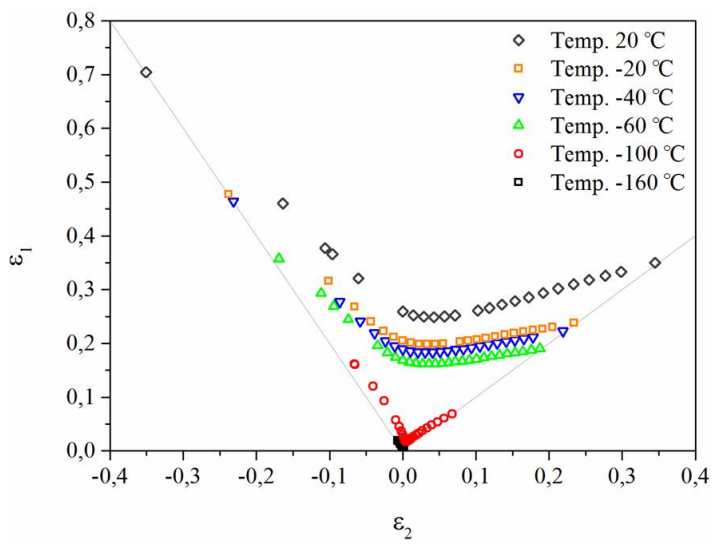

Figure 12. Failure limit curves at each temperature giving critical combinations of the in-plane principal strains ε_1 and ε_2 under proportional loading.

5.2 Influence of fictitious plate size

The SED criterion was calibrated based on detailed simulations of a fictitious plate (P2) with a through-thickness crack in the centre. The size of the 10 mm thick plate was $70 \times 70\ \mathrm{mm}^2$. A shell element (P1) of the same size was used to calculate the critical value of the SED at failure of the plate for a range of stress states and temperatures. Since the size of the plate is large compared with the thickness, the local deformations in the central region due to local necking and damage evolution should have only minor effects on the calibrated values of the SED criterion. However, if the size of the plate is reduced, local deformations will start to play a role and increased values

of the critical SED are expected, in particular for the ductile failure modes. To investigate the influence of plate size on the calibrated values of the SED criterion, simulations with different size of the two square plates P1 and P2 were run, everything else being the same. The simulations are carried out for plane-strain conditions only, assuming the results to be representative for other stress states also. The plate length is taken in the range from 1 to 5 times the plate thickness, namely 10 mm, 15 mm, 20 mm, 30 mm, and 50 mm. Figure 13 shows the resulting values of w_c as a function of the plate size for different temperatures. When the failure mode is still ductile, w_c decreases notably with the plate length but seems to saturate at a length in the range of 40-70 mm. The decrease is largest at room temperature, while the plate size dependence disappears at $-100℃$ where the failure mode is brittle.

The numerical simulations show that the strains localize into a narrow neck in the middle of plate P2 when the failure mode is ductile. The degree of local necking is continuously reduced with decreasing temperature and at $-100℃$ failure occurs without significant necking. It is well known that the strains develop locally into a narrow neck after the onset of local instability and that the width of the neck is set by the plate thickness [61]. Shell elements with size larger than the thickness of the plate are not able to capture local necking, and it is reasonable to assume that failure of the shell element occurs simultaneously with incipient local necking. This is the idea behind the BWH criterion [31] and is obtained also with the SED criterion provided the plate size used in the calibration is sufficiently large compared with the plate thickness and the size of the crack. Based on Figure 13, the size of the fictitious plate used in the calibration should be at least four times its thickness to ensure conservative estimates on the critical SED at room temperature.

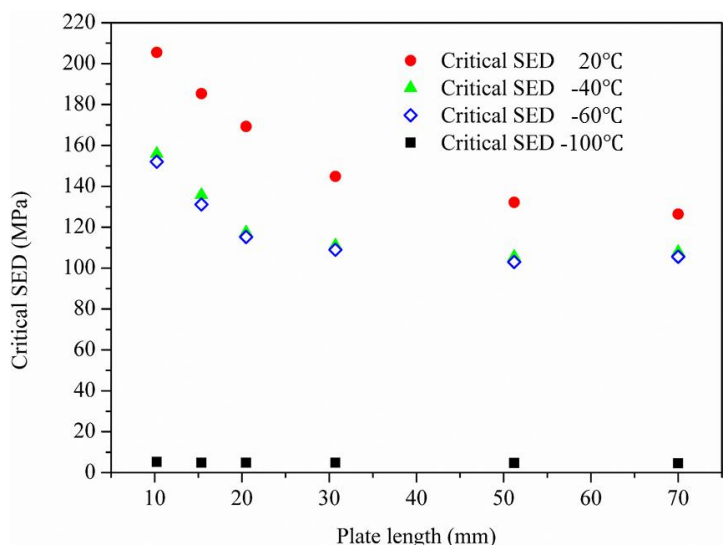

Figure 13. Critical strain energy density (SED) as a function of plate length for plane-strain tension

6 Numerical study

For practical assessment of the proposed modelling approach, using the SED criterion to model failure in large shell elements at low temperatures, a numerical study is performed and the predictions are compared with experimental results from the literature. Park et al. [9] and Kim et al. [35] conducted experiments to examine the impact response of steel-plated structures in Arctic temperatures. The steel-plated structure was subjected to high-speed impact by a cone-shaped striker. Both unstiffened and stiffened plates were tested. In the stiffened plates, two stiffeners were welded across the rear side of the plate. The dimensions of the plate and the flat-type stiffener were $1200 \times 1200 \times 6\ \mathrm{mm}^3$ and $1200 \times 100 \times 6\ \mathrm{mm}^3$, respectively. The edges of the plate were welded to a rigid jig, which was fully clamped by means of bolts. The mass of the cone-shaped striker was 1150 kg. The striker impacted the centre of the plate and its initial velocity at the moment of impact was 7.06 m/s and 8.57 m/s for room temperature and sub-zero temperatures, respectively. The target temperatures were $20℃$, $-40℃$, $-60℃$ and $-100℃$. Table 3 compiles the experimental programme. A detailed description of the test setup can be found in References [9] and [35].

Table 3. Experimental programme from References [9] and [35].

Case	Plate type	Temperature (℃)	Striker velocity (m/s)
1	Unstiffened	20	7.06
2	Stiffened		
3	Unstiffened	-40	8.57
4	Stiffened	-60	
5	Unstiffened	-60	
6	Stiffened	-100	

6.1 Finite element modelling

To simulate the impact tests, the commercial FEA program ABAQUS/explicit was used. The test jig was discretized using solid elements (C3D8R). The cone-shaped striker was assumed to be a rigid body and modelled using four-node 3D bilinear rigid quadrilateral elements (R3D4). The test structure, including the plate and the stiffeners, was modelled using shell elements (S4R). The number of integration point across the thickness was five. The element size was $20 \times 20\ \mathrm{mm}^2$, in accordance with a mesh convergence study conducted in references [9] and [35] to reduce the computation time as much as possible while still getting accurate results. The welds could not be directly modelled by means of shell finite elements. The welds increase the resistance of the

stiffener and make the transition between stiffener and plate less abrupt. Adopting the approach in [35, 62-64], the welds were accounted for by increasing the element thickness around the plate-stiffener junction by 50%, as shown in Figure 14. The friction coefficient was set to 0.3 for all contact surfaces. The FE modelling of the test setup is shown in Figure 15.

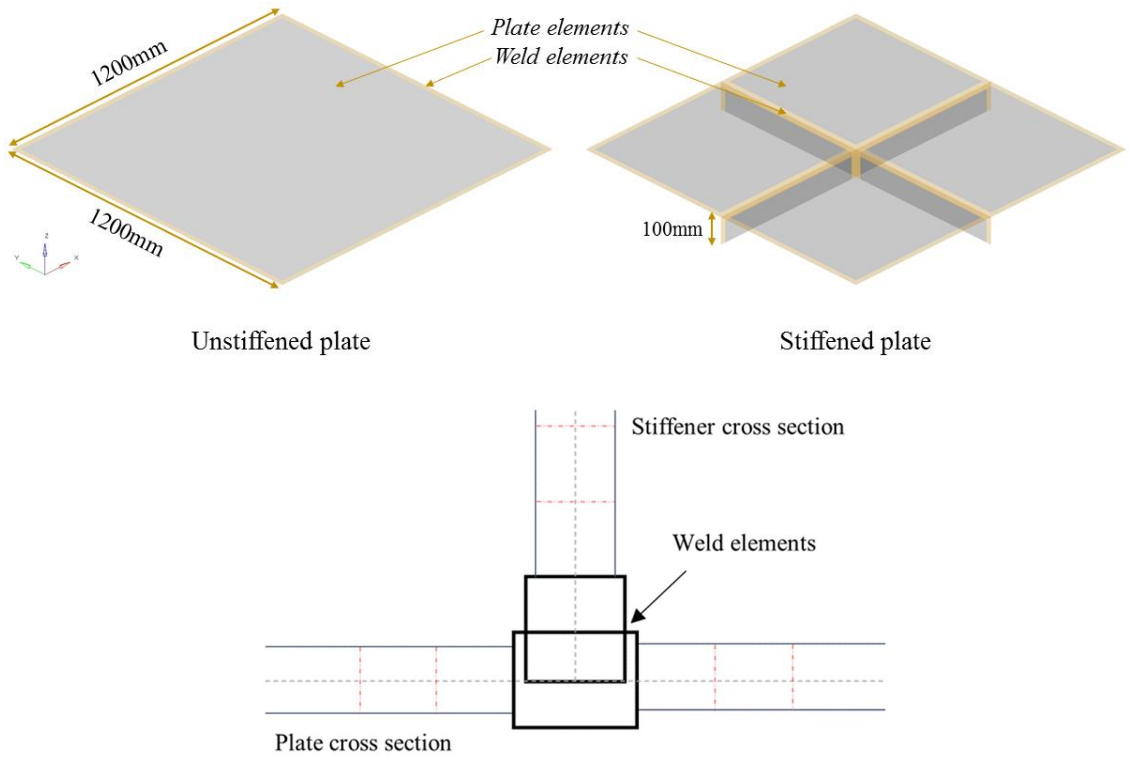

Figure 14. Illustration of plate types and weld elements in the plate-stiffener junction.

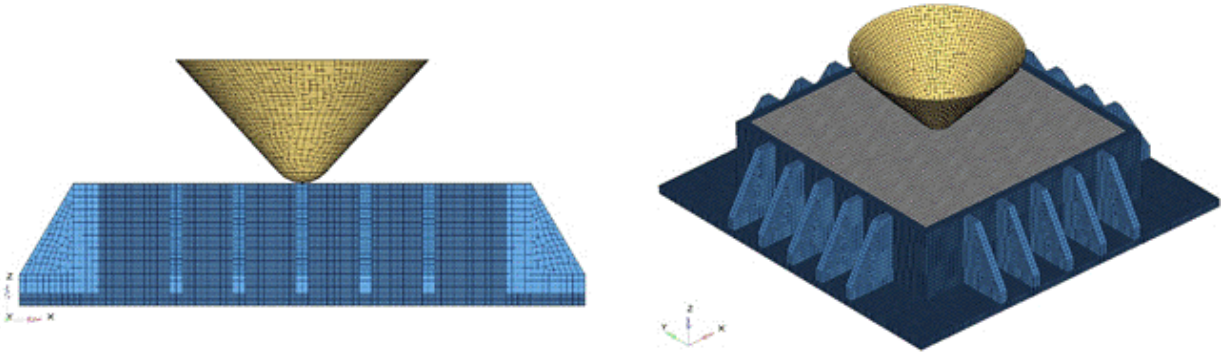

Figure 15. Finite element modelling of the dropped-object tests in [9] and [35].

6.2 Material modelling

We use the stress-strain curves shown in Figure 2 for the behaviour of the steel material in the numerical analyses. The material model combining von Mises plasticity with the SED failure criterion was implemented in the ABAQUS/explicit code via a user-material subroutine VUMAT. To integrate the constitutive equations, the cutting plane algorithm was adopted, which is an accurate, robust and efficient for integrating rate-independent plasticity models [65].

The failure condition is checked after the stress update is fully completed in each time step. If the SED in an element exceeds the pre-defined upper limit value at a certain temperature, i.e., if $w \geq w_c(\beta, T)$, the element is deleted. The criterion for element deletion distinguishes between predominantly ductile and brittle failure modes. For ductile failure modes, the element is not deleted before the critical value, w_c, is achieved in the middle integration point through the thickness. Accordingly, for a bending dominated stress state, the failure of integration points propagate from the surface to the mid integration point, and then the element is completely removed. For brittle failure modes, it is assumed that fracture initiates and propagates instantaneously once the first integration point reaches the critical value. Based on the fracture behaviour of plate P2 in the calibration of the SED criterion, it was concluded that predominant ductile failure modes occurred for temperatures between $20°\mathrm{C}$ and $-60°\mathrm{C}$, while brittle failure modes were found for temperatures equal to and below $-100°\mathrm{C}$. Thus, for $T \leq -100°\mathrm{C}$, an element will be eroded once the first through-thickness integration point fails.

It is important to note that in line with the calibration of the SED criterion and the local modelling of fracture, the strain rate effects have been neglected in the numerical simulations of the impact tests. Kim et al. [35] found from tension coupon tests at room temperature and at $-60°\mathrm{C}$ that the temperature had a significantly larger impact on the tensile strength than the strain rate in the range of 0.1 to 2 s^{-1}. The strain rate had a more significant effect on the lower yield strength. The tests showed also that the fracture strain decreased for higher strain rates. It will be very challenging and require a substantial number of material tests to include the rate effect on the complete stress-strain relationship including lower yield strength, tensile strength, initiation of diffuse necking and fracture. Noticing that the tensile strength was little influenced by strain rate, it was decided to disregard the rate effect. This might underestimate the risk of brittle fracture for high strain rate at very small strains corresponding to lower yield strength.

6.3 Numerical results

In the following, numerical results obtained with the proposed failure model are compared with the experimental data from References [9] and [35].

Case 1 & 2

As shown in Figure 16, the predicted force-displacement curves are in good agreement with the experimental curves both for the unstiffened and stiffened plates loaded at room temperature. While the spring-back is underestimated for the unstiffened plate (case 1), it is quite accurately captured for the stiffened plate (case 2). Material failure did not occur in the tests at room

temperature and the same holds true for the simulations. The impact load yields a fairly constant stress state in the range from $\beta \approx 0.7$ to equi-biaxial tension ($\beta \approx 1.0$) near the elements in contact with the striker. Selected deformed configurations of the plate are shown in Figure 17 and Figure 18 for case 1 and 2, respectively. In case 1, plastic instability occurs at point 3 according to the BWH criterion (see Figure 16 (left)), but the instability does not develop into failure. In case 2, the largest strain is observed in the stiffeners (see Figure 18), but the BWH criterion does not predict any plastic instability. It is found that the stiffened plate has less global deformation, but absorbs more energy than the unstiffened plate. The deformation modes obtained in tests and simulations are compared in Figure 19, and the agreement is satisfactory.

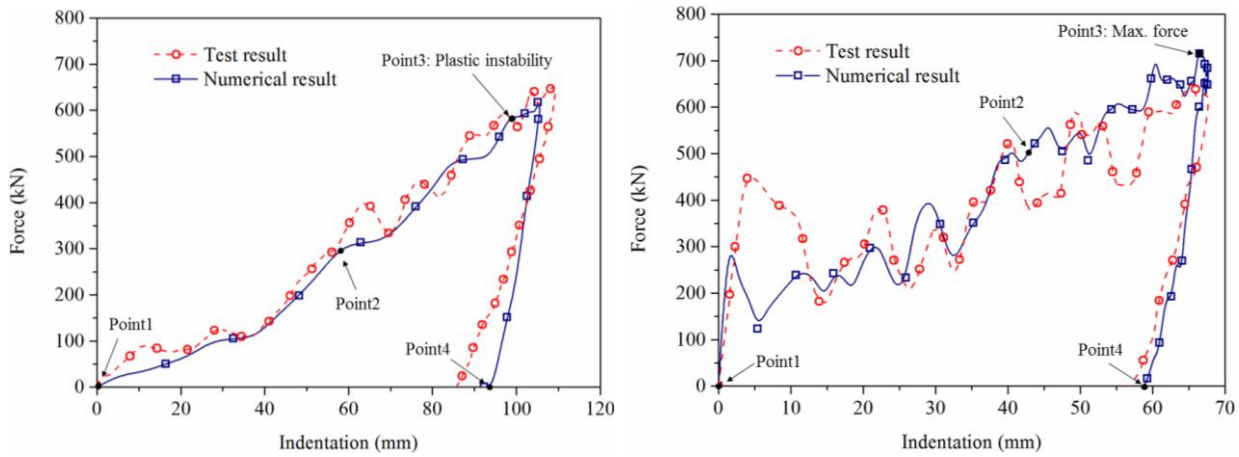

Figure 16. Experimental and numerical force-displacement curves for case 1 (left) and case 2 (right).

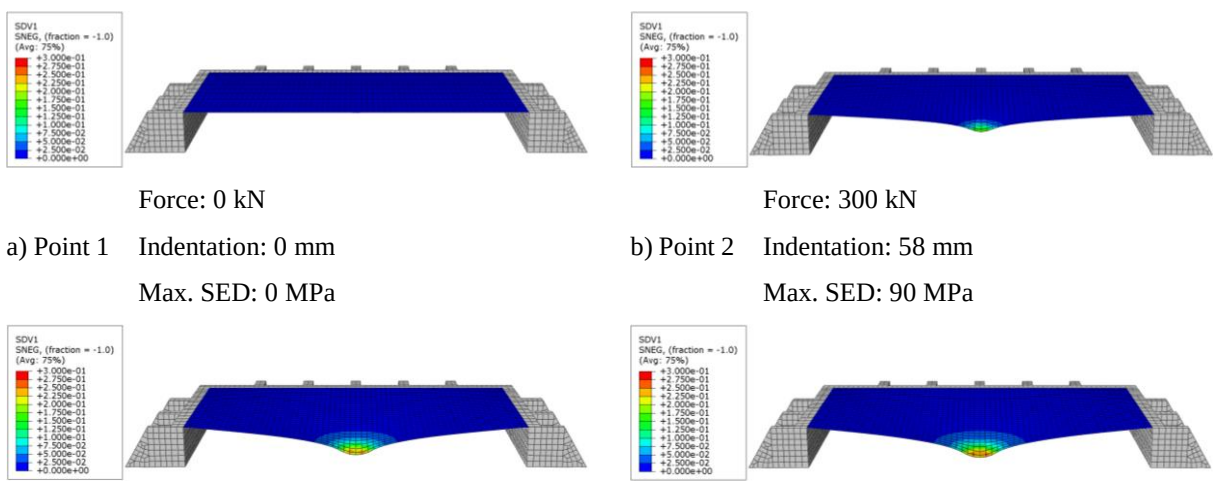

a) Point 1 — Force: 0 kN; Indentation: 0 mm; Max. SED: 0 MPa

b) Point 2 — Force: 300 kN; Indentation: 58 mm; Max. SED: 90 MPa

c) Point 3 — Force: 581 kN; Indentation: 98 mm; Max. SED: 147 MPa

d) Point 4 — Force: 0 kN; Indentation: 94 mm; Max. SED: 165 MPa

Figure 17. Deformed configurations of plate in case 1 with fringe plots of the equivalent plastic strain field. Force, indentation and maximum SED are given for each point which refers back to the force-displacement curve in Figure 16 (left).

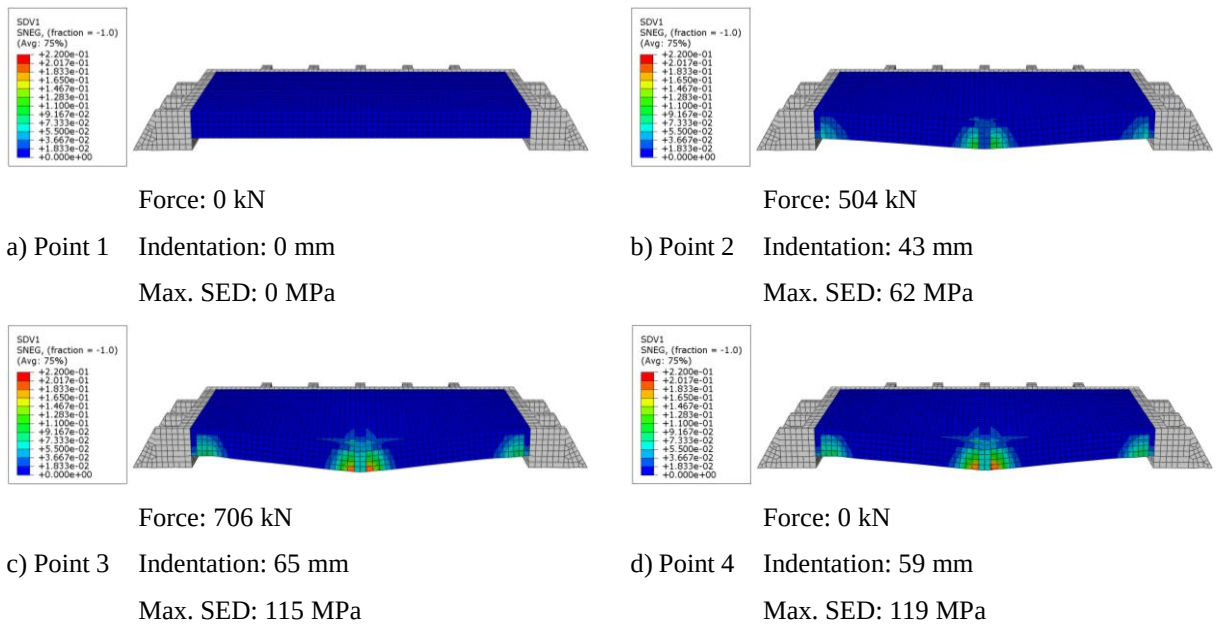

a) Point 1 Force: 0 kN Indentation: 0 mm Max. SED: 0 MPa

b) Point 2 Force: 504 kN Indentation: 43 mm Max. SED: 62 MPa

c) Point 3 Force: 706 kN Indentation: 65 mm Max. SED: 115 MPa

d) Point 4 Force: 0 kN Indentation: 59 mm Max. SED: 119 MPa

Figure 18. Deformed configurations of plate in case 2 with fringe plots of the equivalent plastic strain field. Force, indentation and maximum SED are given for each point which refers back to the force-displacement curve in Figure 16 (right).

Case 3 & 4

The force-displacement curves from test case 3 and 4, in which the specimens were loaded at a temperature of $-40℃$ and $-60℃$, respectively, are shown in Figure 20. The simulation accurately predicts the experimental force level in case 3, but the spring-back still has a minor deviation. Plastic instability according to the BWH criterion occurs at point 1 (Figure 20 (left)). However, the force continues to increase after this point until maximum indentation. Failure occurs neither in the test nor in the simulation, and the plate remains ductile at $-40℃$. The SED criterion is reliable for the unstiffened plate at this temperature. The deformed configurations of the plate at point 1 (plastic instability) and at point 2 are shown in Figure 21.

In case 4, fracture initiates in the experiment and then propagates along the weld line [35], while neither plastic instability nor failure is predicted in the simulation. At the end of the impact, the maximum SED (175 MPa) is located in the elements in the stiffeners that experience the largest strains, see Figure 22. The elements have a strain increment ratio $\beta \approx -0.4$, where the critical SED is 208 MPa, so initiation of fracture is fairly close at these points. In contrast, fracture took

place in the HAZ in the experiment. At the same deformation level, the elements in the HAZ experience a strain increment ratio β close to 0.8 and the maximum SED is 79 MPa, which is far less than the critical SED of 219 MPa. As a result, the maximum indentation is significantly underestimated, and the deformation modes obtained in the test and the simulation are different, as illustrated in Figure 23. The critical SED at $-60℃$ would have to be scaled by a factor of 0.2 in order to produce the observed brittle facture modes in the HAZ. Alternatively, a temperature of $-100℃$ would also give the correct critical SED. It is obvious that there exists a stress concentration factor due to the presence of the stiffener that is difficult to include for coarse shell element meshes. This is the same challenge we are faced with in the ductile failure domain. In addition, the results may indicate a possible deterioration of the weld properties at low temperatures and thus the behaviour of the weld must be predicted carefully. For the dropped-object tests, detailed measurements of crack sizes in the parent material and the weld properties are not available. If the SED criterion had been calibrated for different the crack sizes, the required crack size to obtain the observed behaviour could have been determined. However, these simulations illustrate the sensitivity of the model in the ductile-to-brittle fracture transition region. The correct trend is obtained, but further verification is needed with more controlled test conditions.

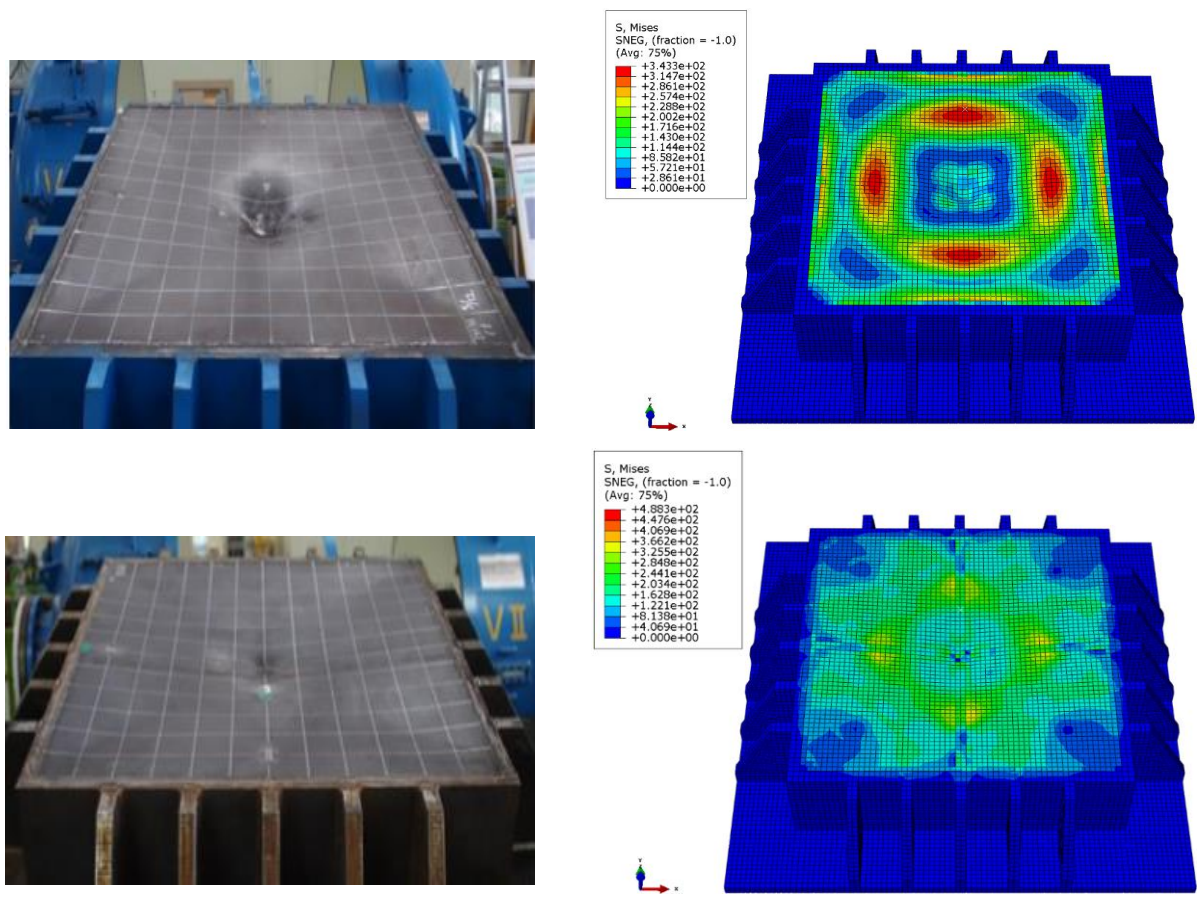

Figure 19. Comparison of experimental and predicted deformation modes for case 1 (top) and case

2 (bottom). The fringe plots show the von Mises stress field (in MPa) at the end of the simulations.

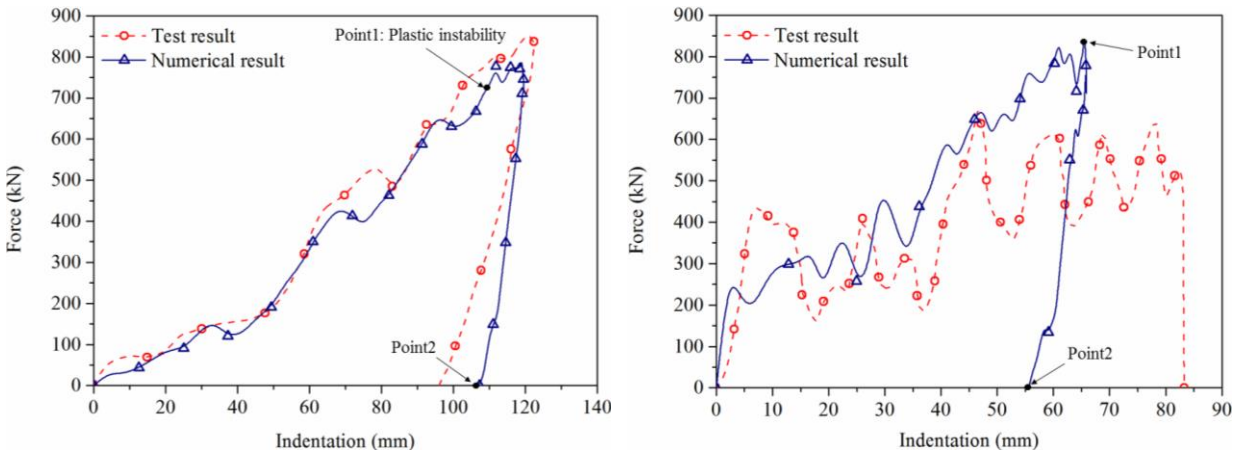

Figure 20. Experimental and numerical force-displacement curves for case 3 (left) and case 4 (right).

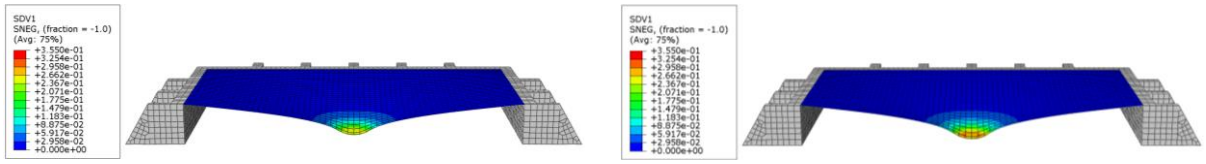

	Force: 712 kN		Force: 0 kN
a) Point 1	Indentation: 108 mm	b) Point 2	Indentation: 107 mm
	Max. SED: 191 MPa		Max. SED: 237 MPa

Figure 21. Deformed configurations of plate in case 3 with fringe plots of the equivalent plastic strain field. Force, indentation and maximum SED are given for each point which refers back to the force-displacement curve in Figure 20 (left).

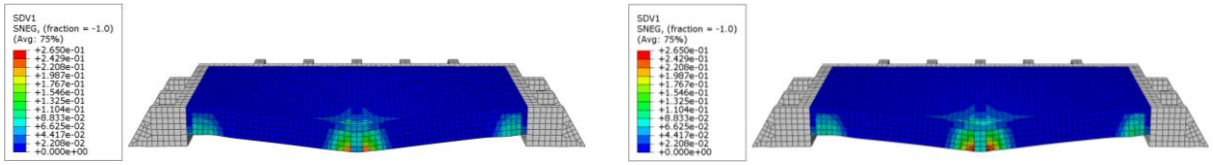

	Force: 847 kN		Force: 0 kN
a) Point 1	Indentation: 66 mm	b) Point 2	Indentation: 56 mm
	Max. SED: 155 MPa		Max. SED: 175 MPa

Figure 22. Deformed configurations of plate in case 4 with fringe plots of the equivalent plastic strain field. Force, indentation and maximum SED are given for each point which refers back to

the force-displacement curve in Figure 20 (right).

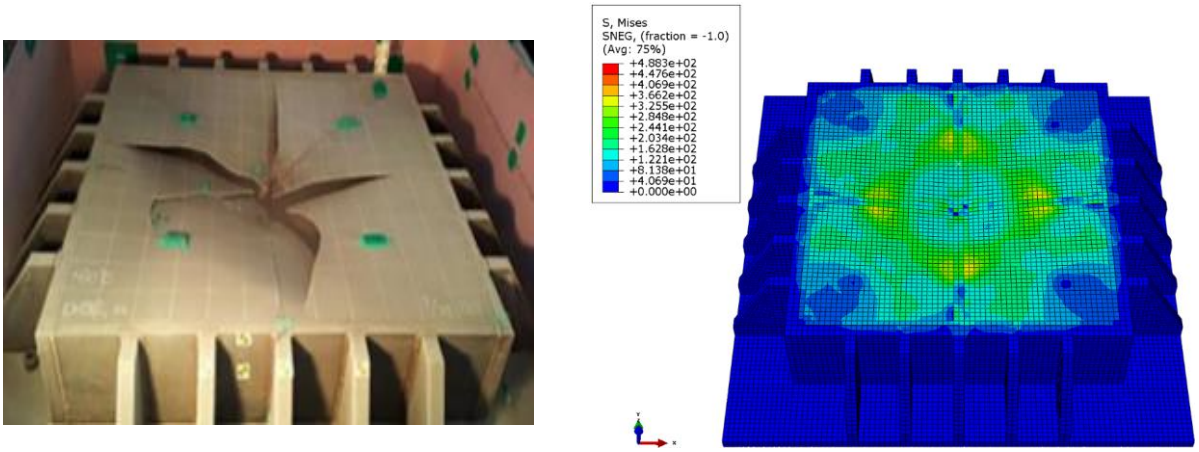

Figure 23. Comparison of experimental and predicted deformation mode for case 4. The fringe plots show the von Mises stress field (in MPa) at the end of the simulations.

Case 5

The force-displacement curves for case 5, where the unstiffened plate is impacted at a temperature of -60℃, are shown in Figure 24. Failure did not occur in the test at this temperature. In the simulation, the elements in the critical region are loaded with a strain increment ratio β close to 0.73, where the critical SED is 205 MPa. The simulation predicts accurately the experimental force level, but in contrast to the test, material failure occurs at point 1 and the maximum indentation is therefore overestimated. The deformed configurations of the plate at maximum force (point 1) and at the end of the simulation (point 2) are shown in Figure 25. Evidently, the simulation predicts failure of elements directly in contact with the striker. Figure 26 compares the deformation modes obtained in the test and the simulation of case 5.

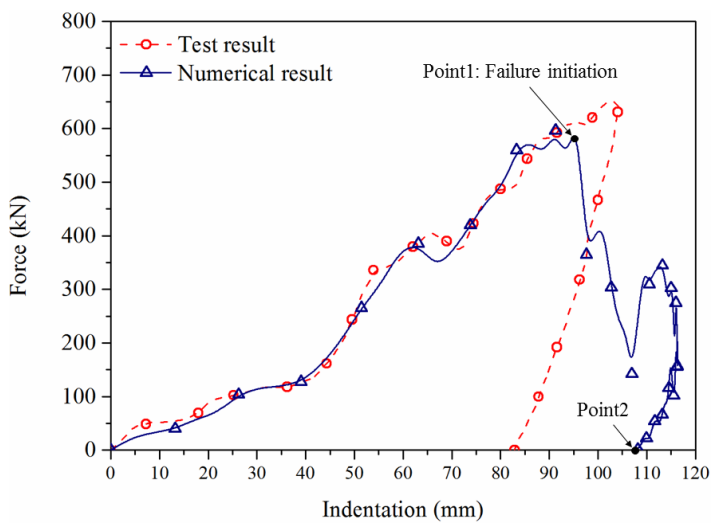

Figure 24. Experimental and numerical force-displacement curves for case 5.

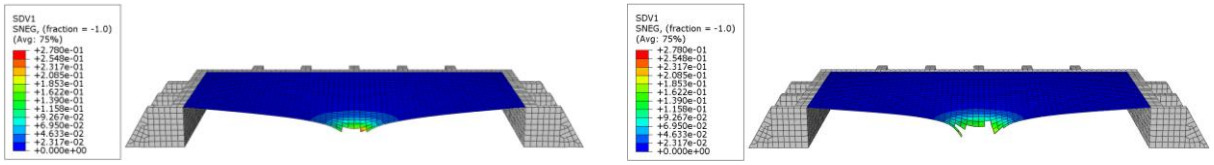

	Force: 586 kN		Force: 0 kN
a) Point 1	Indentation: 96 mm	b) Point 2	Indentation: 108 mm
	Max. SED: 205 MPa		Max. SED: 131 MPa

Figure 25. Deformed configurations of plate in case 5 with fringe plots of the equivalent plastic strain field. Force, indentation and maximum SED are given for each point which refers back to the force-displacement curve in Figure 24.

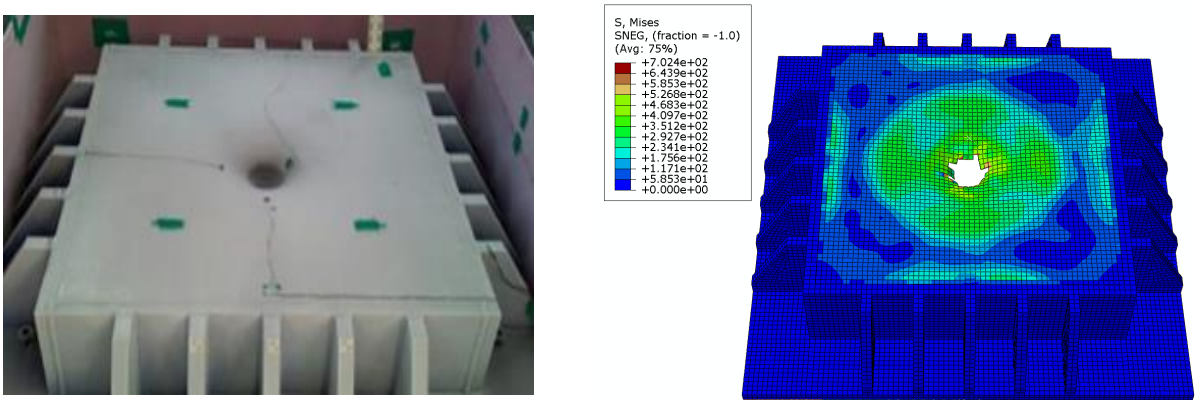

Figure 26. Comparison of experimental and predicted deformation mode for case 5. The fringe plots show the von Mises stress field (in MPa) at the end of the simulations.

Case 6

Figure 27 presents the force-displacement curves for case 6 in which the test of the stiffened plate was performed at $-100℃$. Brittle failure is observed in the test. Failure takes place not only in the area around the plate-stiffener junction, but also on the free plate field with approximately circular shape. The SED criterion predicts failure at about the correct force level, but crack propagation is delayed compared with the test and, accordingly, the post-fracture force level is overestimated. As noticed in case 4, the weld may be prone to fail prematurely at low temperature and could influence the response of the plate. Nevertheless, the fracture pattern of the plate is reasonably well predicted, as illustrated in Figure 28, which presents the final configuration of the

plate in test and simulation. The simulated crack initiation and propagation is depicted in Figure 29. It is evident that brittle fracture is predicted in the simulation, but the strong influence of the discretization is noted.

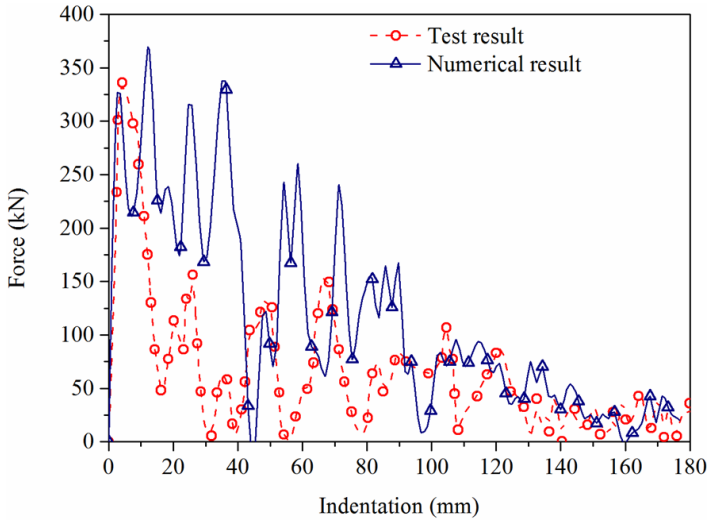

Figure 27. Experimental and simulated force-displacement curves for case 6.

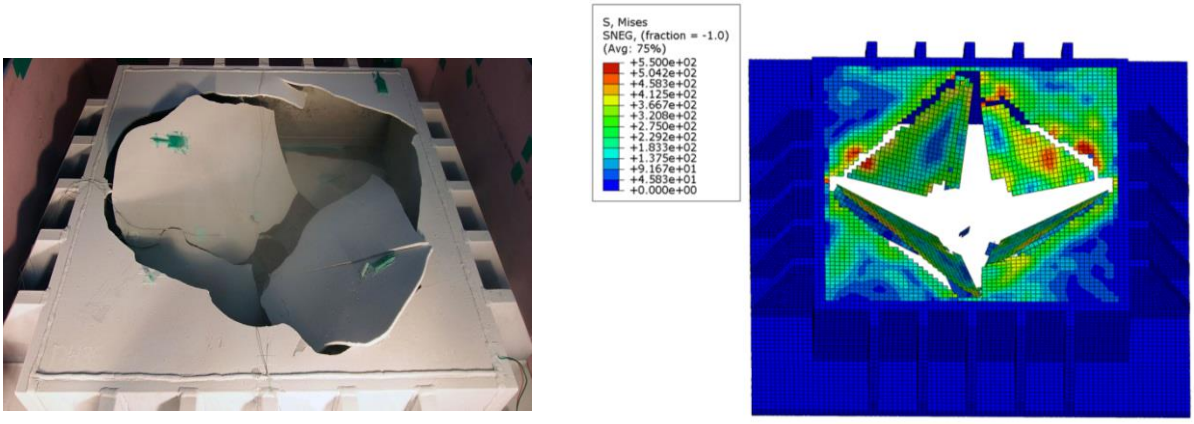

Figure 28. Comparison of experimental and predicted deformation mode for case 6. The fringe plot shows the von Mises stress field (in MPa) at the end of the simulation.

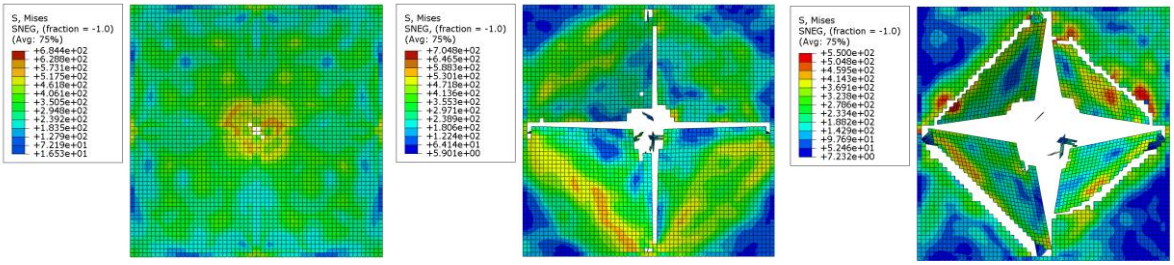

Figure 29. Simulated crack propagation in the stiffened plate at a temperature of −100℃. The fringe plots show the von Mises stress field (in MPa).

The total energy absorption in tests and simulations is compiled in Table 4. In case 1, 2 and 3, the simulations give satisfactory agreement with the tests, while large errors are found in case 6 involving pronounced brittle fracture. The discrepancy is caused by the delayed crack initiation and propagation in the simulation. The comparison for case 4 and 5 is deliberately omitted because the failure mode was not predicted correctly.

Table 4. The total energy absorption of the structure in each case.

Case	Experiment (kJ)	FEA (kJ)	Error (%)
1	25.8	23.8	-7.6
2	24.5	24.4	-0.7
3	37.0	36.3	-1.9
6	11.4	23.6	106.8

7 Discussion and conclusions

Ships and offshore structures may be subjected to extreme actions where the steel material is exposed to very low temperatures, e.g. due to ship or ice impacts in the Arctic or temperature stresses induced by cryogenic spills. During these actions the structure may undergo ductile or brittle fracture. The occurrence of the latter event may be particularly critical. Realistic analysis for large structural subsystems by means of the nonlinear finite element method where ductile and brittle fracture is taken into account, is therefore essential. Numerical simulations require large shell elements, typically in the range of 3-5 times the plate thickness, where detailed modelling of crack initiation and propagation is not feasible.

In the present paper, the strain energy density (SED) criterion was proposed to predict ductile-brittle fracture transition in nonlinear finite element analyses using large shell elements. Critical values of the SED were determined based on local simulations of fracture for a range of temperatures and plane-stress states based on the combined use of the Gurson model for ductile

damage and fracture and the Richie-Knott-Rice (RKR) criterion for brittle fracture. In order to evaluate the proposed model, six drop tests on stiffened and unstiffened steel plates carried out at room temperature and sub-zero temperatures were analysed with shell finite elements and the SED criterion. In some of the drop tests, the steel plate exhibited a ductile behaviour, whereas in others its behaviour was more brittle. The simulations of the drop tests illustrated the feasibility of the SED, even if there were significant differences between tests and simulations in some of the cases. The plate behaviour against impact was predicted quite well for the unstiffened plates, whereas the weld failure occurring at sub-zero temperatures was not captured in the simulations. For the stiffened plates, there are two effects that push the failure mode towards more brittle fracture than it was possible to simulate at the present stage:

1) The stiffener and the welds caused a significant stress and strain concentration that was not taken into account in the shell finite element modelling. It could be taken into account by introducing a stress concentration factor in a similar manner as in the BWH ductile failure model [29].

2) The residual stresses in the HAZ are generally considered to attain the yield stress level. The HAZ material will be heavily stressed and may thus more easily attain the critical SED by low temperature exposure. This may possibly be taken into account by reducing the critical SED for HAZ elements.

The need to carry out dedicated low temperature tests of stiffened and unstiffened plates with better controlled conditions is acknowledged. Preferably, the initial tests should be static, so as to eliminate the uncertain strain rate effects. The verification study was also made difficult because the number of temperature levels is small. The critical SED changes rapidly from $-60℃$ to $-100℃$ (cf. Figure 11). Thus the occurrence of brittle failure or ductile failure is somewhat "binary" and it is difficult to know how close in terms of temperature level the numerical simulations are to the correct behaviour.

Acknowledgement

This work has been funded by the Research Council of Norway (NFR) through the Centers of Excellence funding scheme, project AMOS (Grant number 223254), and the Centers for Research-based Innovation funding scheme, project CASA (Grant number 237885), at the Norwegian University of Science and Technology (NTNU). This support is gratefully acknowledged by the authors.

References

[1] GISIS I. IMO GISIS - Global Integrated Shipping Information System. 2016.

[2] Paik J. Practical techniques for finite element modeling to simulate structural crashworthiness in ship collisions and grounding (Part I: Theory). Ships and Offshore Structures. 2007;2:69-80.

[3] Ehlers S. The influence of the material relation on the accuracy of collision simulations. Marine Structures. 2010;23:462-74.

[4] Ehlers S, Østby E. Increased crashworthiness due to arctic conditions–The influence of sub-zero temperature. Marine Structures. 2012;28:86-100.

[5] Hogström P, Ringsberg JW. An extensive study of a ship's survivability after collision–A parameter study of material characteristics, non-linear FEA and damage stability analyses. Marine structures. 2012;27:1-28.

[6] Choung J, Nam W, Lee J-Y. Dynamic hardening behaviors of various marine structural steels considering dependencies on strain rate and temperature. Marine Structures. 2013;32:49-67.

[7] Storheim M, Amdahl J. On the Effect of Work Hardening on Strain-Localization and Fracture Initiation in Collision Simulations. ASME 2015 34th International Conference on Ocean, Offshore and Arctic Engineering: American Society of Mechanical Engineers; 2015. p. V003T02A-VT02A.

[8] Park DK, Kim DK, Seo JK, Kim BJ, Ha YC, Paik JK. Operability of non-ice class aged ships in the Arctic Ocean-part II: Accidental limit state approach. Ocean Engineering. 2015;102:206-15.

[9] Park DK, Kim KJ, Lee JH, Jung BG, Han X, Kim BJ, et al. Collision Tests on Steel-Plated Structures in Low Temperature. ASME 2015 34th International Conference on Ocean, Offshore and Arctic Engineering: American Society of Mechanical Engineers; 2015. p. V003T02A12-VT02A12.

[10] Nam W, Amdahl J, Hopperstad OS. Influence of brittle fracture on the crashworthiness of ships and offshore structures in Arctic conditions. Proceedings of the ICCGS. 2016;15.

[11] Min D-K, Shin D-W, Kim S-H, Heo Y-M, Cho S-R. On the Plastic Deformation of Polar-Class Ship's Single Frame Structures Subjected to Collision Loadings. Journal of the Society of Naval Architects of Korea. 2012;49:232-8.

[12] Ritchie RO, Knott JF, Rice J. On the relationship between critical tensile stress and fracture toughness in mild steel. Journal of the Mechanics and Physics of Solids. 1973;21:395-410.

[13] Tvergaard V, Needleman A. Effect of material rate sensitivity on failure modes in the Charpy V-notch test. Journal of the Mechanics and Physics of Solids. 1986;34:213-41.

[14] Tvergaard V, Needleman A. An analysis of the brittle-ductile transition in dynamic crack growth. International Journal of Fracture. 1993;59:53-67.

[15] Needleman A, Tvergaard V. Numerical modeling of the ductile-brittle transition. International Journal of Fracture. 2000;101:73-97.

[16] Batra R, Lear M. Simulation of brittle and ductile fracture in an impact loaded prenotched plate. International Journal of Fracture. 2004;126:179-203.

[17] Hütter G, Linse T, Roth S, Mühlich U, Kuna M. A modeling approach for the complete ductile–brittle transition region: cohesive zone in combination with a non-local Gurson-model. International Journal of Fracture. 2014;185:129-53.

[18] Türtük İ, Deliktaş B. Coupled porous plasticity–Continuum damage mechanics approaches for modelling temperature driven ductile-to-brittle transition fracture in ferritic steels. International Journal of Plasticity. 2016;77:246-61.

[19] Gurson AL. Continuum theory of ductile rupture by void nucleation and growth: Part I—Yield criteria and flow rules for porous ductile media. Journal of engineering materials and technology. 1977;99:2-15.

[20] Chu C, Needleman A. Void nucleation effects in biaxially stretched sheets. Journal of engineering materials and technology. 1980;102:249-56.

[21] Tvergaard V, Needleman A. Analysis of the cup-cone fracture in a round tensile bar. Acta metallurgica. 1984;32:157-69.

[22] Xue L. Constitutive modeling of void shearing effect in ductile fracture of porous materials. Engineering Fracture Mechanics. 2008;75:3343-66.

[23] Nahshon K, Hutchinson J. Modification of the Gurson model for shear failure. European Journal of Mechanics-A/Solids. 2008;27:1-17.

[24] Butcher C, Chen Z, Bardelcik A, Worswick M. Damage-based finite-element modeling of tube hydroforming. International journal of fracture. 2009;155:55-65.

[25] Beremin F, Pineau A, Mudry F, Devaux J-C, D'Escatha Y, Ledermann P. A local criterion for cleavage fracture of a nuclear pressure vessel steel. Metallurgical transactions A. 1983;14:2277-87.

[26] Wallin K. Master curve analysis of the "Euro" fracture toughness dataset. Engineering Fracture Mechanics. 2002;69:451-81.

[27] Minami F, Ohata M, Shimanuki H, Handa T, Igi S, Kurihara M, et al. Method of constraint loss correction of CTOD fracture toughness for fracture assessment of steel components. Engineering Fracture Mechanics. 2006;73:1996-2020.

[28] Tørnqvist R. Design of Crashworthy Ship Strucures. 2003.

[29] Servis D, Samuelides M. Implementation of the T-failure criterion in finite element methodologies. Computers & structures. 2006;84:196-214.

[30] Bai Y, Wierzbicki T. A new model of metal plasticity and fracture with pressure and Lode dependence. International journal of plasticity. 2008;24:1071-96.

[31] Alsos HS, Amdahl J, Hopperstad OS. On the resistance to penetration of stiffened plates, Part II: Numerical analysis. International Journal of Impact Engineering. 2009;36:875-87.

[32] Storheim M, Alsos HS, Hopperstad OS, Amdahl J. A damage-based failure model for coarsely meshed shell structures. International Journal of Impact Engineering. 2015;83:59-75.

[33] Veritas DN. DNV-OS-B101 : Metallic Materials. 2015.

[34] Sumpter J, Kent J. Fracture toughness of grade D ship steel. Engineering fracture mechanics. 2006;73:1396-413.

[35] Kim KJ, Lee JH, Park DK, Jung BG, Han X, Paik JK. An experimental and numerical study on nonlinear impact responses of steel-plated structures in an Arctic environment. International Journal of Impact Engineering. 2016;93:99-115.

[36] Tvergaard V. Influence of voids on shear band instabilities under plane strain conditions. International Journal of Fracture. 1981;17:389-407.

[37] Anderson TL. Fracture mechanics: fundamentals and applications: CRC press; 2017.

[38] Orowan E. Fracture and strength of solids. Reports on progress in physics. 1949;12:185.

[39] Knott J. Some effects of hydrostatic tension on the fracture behaviour of mild steel. J Iron Steel Inst. 1966;204:104-11.

[40] Sih GC. Strain-energy-density factor applied to mixed mode crack problems. International Journal of fracture. 1974;10:305-21.

[41] Sih G, Ho J. Sharp notch fracture strength characterized by critical energy density. Theoretical and Applied Fracture Mechanics. 1991;16:179-214.

[42] Wei Y. An extended strain energy density failure criterion by differentiating volumetric and distortional deformation. International Journal of Solids and Structures. 2012;49:1117-26.

[43] Cao J, Li F, Li P, Ma X, Li J. Analysis of ductile–brittle competitive fracture criteria for tension process of 7050 aluminum alloy based on elastic strain energy density. Materials Science and Engineering: A. 2015;637:201-14.

[44] Shen WQ, Jones N. A failure criterion for beams under impulsive loading. International Journal of Impact

Engineering. 1992;12:101-21.

[45] Shen WQ, Jones N. Dynamic plastic response and failure of a clamped beam struck transversely by a mass. International journal of solids and structures. 1993;30:1631-48.

[46] Choung J. Comparative studies of fracture models for marine structural steels. Ocean Engineering. 2009;36:1164-74.

[47] Sumpter J, Kent J. Prediction of ship brittle fracture casualty rates by a probabilistic method. Marine structures. 2004;17:575-89.

[48] E1921-97 A. Standard test method of determination of reference temperature, T_0, for ferritic steels in the transition range.

[49] Knott J. On stress intensifications in specimens of Charpy geometry prior to general yield. Journal of the Mechanics and Physics of Solids. 1967;15:97-103.

[50] Alsos HS, Amdahl J. On the resistance of tanker bottom structures during stranding. Marine Structures. 2007;20:218-37.

[51] Mai QA, Sørensen JD, Rigo P. Updating Failure Probability of a Welded Joint in Offshore Wind Turbine Substructures. ASME 2016 35th International Conference on Ocean, Offshore and Arctic Engineering: American Society of Mechanical Engineers; 2016. p. V003T02A59-VT02A59.

[52] Moan T. Development of accidental collapse limit state criteria for offshore structures. Structural Safety. 2009;31:124-35.

[53] Ziegler L, Schafhirt S, Scheu M, Muskulus M. Effect of load sequence and weather seasonality on fatigue crack growth for monopile-based offshore wind turbines. Energy Procedia. 2016;94:115-23.

[54] Akpan UO, Koko TS, Ayyub B, Dunbar TE. Risk assessment of aging ship hull structures in the presence of corrosion and fatigue. Marine structures. 2002;15:211-31.

[55] Bokalrud T, Karlsen A. Control of Fatigue Failure in Ship Hulls by Ultrasonic Inspection. Norwegian Maritime Research. 1982;10:9-15.

[56] Kountouris I, Baker M. 'Defect Assessment. Analysis of Defects Detected by MPI in an Offshore Structure. CESLIC Report No OR6, Dept Civil Engineering, Imperial College, London, UK. 1989.

[57] Kirkemo F. Applications of probabilistic fracture mechanics to offshore structures. Appl Mech Rev. 1988;41:61-84.

[58] Kõrgesaar M, Tabri K, Naar H, Reinhold E. Ship collision simulations using different fracture criteria and mesh size. ASME 2014 33rd International Conference on Ocean, Offshore and Arctic Engineering: American Society of Mechanical Engineers; 2014. p. V04AT2A045-V04AT02A.

[59] Goodwin GM. Application of strain analysis to sheet metal forming problems in the press shop. SAE technical paper; 1968.

[60] Keeler SP, Backofen WA. Plastic instability and fracture in sheets stretched over rigid punches. Asm Trans Q. 1963;56:25-48.

[61] Storheim M. Structural response in ship-platform and ship-ice collisions. 2016.

[62] Alsos HS, Amdahl J. On the resistance to penetration of stiffened plates, Part I–Experiments. International Journal of Impact Engineering. 2009;36:799-807.

[63] Villavicencio R, Soares CG. Numerical modelling of laterally impacted plates reinforced by free and end connected stiffeners. Engineering Structures. 2012;44:46-62.

[64] Wang T, Hopperstad O, Lademo O-G, Larsen P. Finite element analysis of welded beam-to-column joints in aluminium alloy EN AW 6082 T6. Finite elements in analysis and design. 2007;44:1-16.

[65] Ortiz M, Simo J. An analysis of a new class of integration algorithms for elastoplastic constitutive relations. International Journal for Numerical Methods in Engineering. 1986;23:353-66.